

**Multimode Interference based Mach-Zehnder
Interferometer in SOI Platform for DWDM applications**

A THESIS

submitted by

UPPU KARTHIK

for the award of the degree

of

MASTER OF SCIENCE

(by Research)



**DEPARTMENT OF ELECTRICAL ENGINEERING
INDIAN INSTITUTE OF TECHNOLOGY MADRAS**

JUNE 2013

THESIS CERTIFICATE

This is to certify that the thesis titled “**Multimode Interference based Mach-Zehnder Interferometer in SOI Platform for DWDM applications**”, submitted by **Uppu Karthik**, to the Indian Institute of Technology, Madras, for the award of the degree of **Master of Science**, is a bonafide record of the research work done by him under my supervision. The contents of this thesis, in full or in parts, have not been submitted to any other Institute or University for the award of any degree or diploma.

Dr. Bijoy K. Das
Research Guide
Associate Professor
Dept. of Electrical Engineering
IIT-Madras, India, 600 036

Place: Chennai, India
Date: Tue 16th Jul, 2013

Dedicated to my Parents.

ACKNOWLEDGEMENTS

This thesis acknowledgment gives me an opportunity to thank all those who supported me at various stages of my research work providing motivation, knowledge, help and suggestions whenever I was in need. First and foremost, I would like to thank my mentor Dr. Bijoy K. Das, for providing me with the opportunity to work under his guidance. The personal interaction sessions and group meetings that happened over the period of my project work were truly enlightening and encouraging. I would also like to thank my General Test Committee (GTC) members Prof. E. Bhattacharya, Prof. Hari Shankar Ramchandran, Dr. Deepa Venkitesh, Prof. C. Vijayan, for their valuable suggestions that helped me to fine tune my research work. I am thankful to Electrical Engineering Department, IIT Madras and all the faculty of Microelectronics & MEMS labs for providing me with the required facilities to carry out my experimental work.

My special thanks to the support staff Mr. Prakash, Mr. Rajendran and Mr. Sreedhar for their timely help on various technicalities pertaining to the fabrication and characterization equipment's and setup. I am grateful to all my seniors for teaching me various aspects of fabrication and characterization of integrated optical devices. My special thanks to all the members of Integrated Optoelectronics and, Microelectronics & MEMS Laboratories for their help and valuable suggestions during different stages of my research work. I thank my co-authors of various publications/proceedings, Gaugrang, Rajat and Sujith.

I am grateful to friends at IIT-Madras, for their love and support, which has constantly kept inspiring and encouraging me at various stages of my stay here. Last but not the least, I am grateful to my parents and family for their continuing support that helped me to accomplish this work.

ABSTRACT

Silicon-on-Insulator (SOI) is well established platform for MEMS and CMOS devices. It is also found to be an excellent platform for demonstrating photonic devices integrated with CMOS electronics. Integrated optical Mach-Zehnder Interferometer (MZI) is an important building block used not only for CMOS optical interconnects but also for wavelength filtering/switching applications in passive/active optical networks. However, the performance of SOI based MZI is limited by the waveguide dispersion and polarization dependencies, which can be minimized by proper choice of waveguide geometry and dimensions.

In this work, we present the design and experimental demonstration of a compact 2×2 integrated optical MZI in SOI platform (device layer - $2 \mu m$, BOX - $1 \mu m$, substrate - $500 \mu m$) that shows a nearly dispersion-free response and polarization-independent extinction over a wide wavelength range (C+L optical band). The entire device footprint is $\sim 0.8 \text{ mm} \times 5.2 \text{ mm}$ (W \times L); which is comprised of optimally designed single-mode waveguides (for input/output and interferometer arms) and a pair of multi-mode interference (MMI) based 3-dB power splitters. To monitor the wavelength dependent performance, unbalanced arm lengths ($L \sim 3037 \mu m$, $L+\Delta L \sim 3450 \mu m$) were introduced to construct the MZI. The differential arm length ($\Delta L \sim 412 \mu m$) has been specifically chosen to provide alternate ITU channels (spaced by 100 GHz) transmission peaks at both the output ports alternatively. Using these design parameters, devices were fabricated by photo-lithographic definition and subsequent reactive ion etching process. Finally, the waveguide end-facets were polished carefully for optical characterizations. As expected, the characterization results show that all the devices could separate alternate ITU channels into two output ports. We also observe a uniform channel extinction of $\sim 15 \text{ dB}$ with a 3-dB bandwidth of $\sim 100 \text{ GHz}$ for both polarizations at the output ports over the wavelength range of 1520 nm to 1600 nm.

TABLE OF CONTENTS

| | |
|--|-------------|
| ACKNOWLEDGEMENTS | ii |
| ABSTRACT | iii |
| LIST OF TABLES | vi |
| LIST OF FIGURES | viii |
| ABBREVIATIONS | ix |
| NOTATION | xi |
| 1 Introduction | 1 |
| 1.1 Motivation | 1 |
| 1.2 Research Objective | 5 |
| 1.3 Thesis Organization | 6 |
| 2 Design and Simulations | 7 |
| 2.1 Background Theory | 7 |
| 2.2 Single-mode Waveguide with 2- μm SOI | 9 |
| 2.3 MMI based 3-dB Power Splitter | 14 |
| 2.4 MMI Based 2×2 MZI Structure | 17 |
| 2.5 Conclusions | 24 |
| 3 Photomask and Device Fabrication | 25 |
| 3.1 Mask Design and Fabrication | 25 |
| 3.2 Device Fabrication | 26 |
| 3.3 Waveguide Properties: Experimental Results | 32 |
| 3.4 Conclusions | 35 |

| | | |
|----------|--|-----------|
| 4 | Device Characterizations | 36 |
| 4.1 | MMI Coupler | 36 |
| 4.2 | Mach-Zehnder Interferometer | 38 |
| 4.3 | Conclusions | 43 |
| 5 | Conclusions | 44 |
| 5.1 | Summary | 44 |
| 5.2 | Outlook | 45 |
| A | Appendix | 47 |
| A.1 | Asymmetric MZI Based Interleaver | 47 |
| A.2 | Recipes for etching | 51 |

LIST OF TABLES

| | | |
|-----|---|----|
| 2.1 | Various waveguide geometries in SOI | 9 |
| 2.2 | Calculated waveguide birefringence, mode-size and dispersion slopes for various waveguide structures | 11 |
| 2.3 | Optimized design parameters for single-mode waveguides, 3-dB MMI splitter and MZI based Interleaver structure | 23 |
| 3.1 | List of fabricated samples | 32 |
| 3.2 | Waveguide dimensions and calculated birefringence in different samples | 34 |

LIST OF FIGURES

| | | |
|------|--|----|
| 1.1 | Various interconnect delays with the advancement towards higher technological nodes | 2 |
| 1.2 | IBM proposal of 3-D processor using optical interconnects | 3 |
| 1.3 | Cascaded asymmetric MZIs used for 4-channel WDM filter in CMOS nanophotonic chip | 4 |
| 2.1 | Schematic top-view of an asymmetric MZI | 7 |
| 2.2 | Typical SOI rib waveguide structure | 10 |
| 2.3 | Group index dispersion in SOI waveguides | 11 |
| 2.4 | Single-mode region in W-h plane for RCRW in SOI platform | 12 |
| 2.5 | Structural birefringence ($n_{eff}^{TE} - n_{eff}^{TM}$) as a function of waveguide width for various device layer thicknesses | 13 |
| 2.6 | Birefringence and difference in waveguide mode-size ($1/e$ horizontal spread at $\lambda \sim 1550 \text{ nm}$) for two different polarizations as a function of $r = (h/H)$ | 13 |
| 2.7 | Schematic 3-D view of 2×2 MMI coupler | 16 |
| 2.8 | Transmitted powers in bar port and cross port of MMI based power-splitter as a function of (a) W_{it} and (b) L_{mmi} | 18 |
| 2.9 | Polarization and wavelength dependent characteristics of optimized MMI based 3-dB power splitter | 19 |
| 2.10 | Simulated results of 2×2 MZI structure | 20 |
| 2.11 | Schematic diagram of an 2×2 MZI based interleaver structure showing various design parameters | 21 |
| 2.12 | Simulated transmission characteristics at cross port and bar port of an un-balanced 2×2 MMI based MZI structure for TM polarization | 22 |
| 2.13 | Wavelength and polarization dependent characteristics of an un-balanced 2×2 MMI based MZI structure | 22 |
| 2.14 | Calculated transmission loss of a 90° bend waveguide structure as a function of bend radius for both TE and TM polarizations at $\lambda \sim 1550 \text{ nm}$ | 23 |
| 3.1 | Schematic top view layout used for fabrication of interleaver mask | 26 |

| | | |
|-----|---|----|
| 3.2 | Fabrication process steps | 27 |
| 3.3 | SEM image of waveguide and MMI coupler in a sample without post exposure bake | 29 |
| 3.4 | SEM image of waveguide and MMI coupler in a sample with post exposure bake | 29 |
| 3.5 | SEM images of different sections of a fabricated interleaver | 30 |
| 3.6 | SEM image of polished end-facet of fabricated device | 31 |
| 3.7 | Schematic of an end-fire coupling setup | 33 |
| 3.8 | Transmitted TE and TM mode profiles for single-mode reduced cross-section rib waveguides | 34 |
| 3.9 | Fabry-Perot response for reduced cross-section rib waveguides for TE and TM polarization's | 35 |
| 4.1 | Transmitted intensity profiles for RCRW based multi-mode interference based coupler | 36 |
| 4.2 | Wavelength dependent throughput fraction of power in bar port for RCRW based MMI couplers | 37 |
| 4.3 | Transmitted intensity profiles for interleaver at two wavelengths | 38 |
| 4.4 | Measured wavelength dependent transmission characteristics (C band) at output ports of MMI based MZI | 38 |
| 4.5 | Measured wavelength dependent transmission characteristics TM polarization, at output ports of MZI | 39 |
| 4.6 | Measured wavelength and polarization dependent transmission characteristics at output ports of MZI in device 1. | 39 |
| 4.7 | Measured wavelength and polarization dependent transmission characteristics at output ports of MZI in device IOL-UK4. | 40 |
| 4.8 | Schematic of an characterization setup for recording device response in OSA | 41 |
| 4.9 | OSA response of Broadband source and EDFA with and without MZI | 42 |
| 5.1 | MZI integrated with PIN structure and cascaded lattice type filters using MZI | 45 |

ABBREVIATIONS

Acronyms

| | |
|---------------|--|
| AWG | Arrayed Waveguide Grating |
| Band C | Conventional wavelength band ($\lambda \sim 1527$ to 1567 nm) |
| Band L | Long wavelength band ($\lambda \sim 1567$ to 1607 nm) |
| BOX | Buried Oxide |
| BPM | Beam Propagation Method |
| CMOS | Complementary Metal Oxide Semiconductor |
| DI | De-ionized (water) |
| DWDM | Dense Wavelength Division Multiplexing |
| EDFA | Erbium-doped Fiber Amplifier |
| FSR | Free Spectral Range |
| ICP | Inductively Coupled Plasma |
| ITU | International Telecommunication Union |
| LCRW | Large Cross-section Rib Waveguide |
| MZI | Mach Zehnder Interferometer |
| MMI | Multi-mode Interference |
| OSA | Optical Spectrum Analyzer |
| PhWW | Photonic Wire Waveguide |
| PhWRW | Photonic Wire Rib Waveguide |
| PPR | Positive Photo Resist |
| RCRW | Reduced Cross-section Rib Waveguide |
| RIE | Reactive Ion Etching |
| SEM | Scanning Electron Microscope |
| SMF | Single Mode Fiber |
| SOI | Silicon-On-Insulator |
| TE | Transverse Electric (polarization) |
| TM | Transverse Magnetic (polarization) |

UV Ultra-Violet

Chemical Names

| | |
|-----------------------------------|---------------------|
| Ar | Argon |
| CHF₃ | Tri-fluoro Methane |
| HF | Hydro Fluoric Acid |
| HNO₃ | Nitric Acid |
| H₂O | Water |
| H₂O₂ | Hydrogen Peroxide |
| NaOH | Sodium Hydroxide |
| SF₆ | Sulfur Hexafluoride |
| Si | Silicon |
| SiO₂ | Silicon dioxide |
| TCE | Tri-chloro Ethylene |

Units

| | |
|--------------|--------------------------------------|
| dB | Decibel |
| dBm | Decibel milli-Watts |
| mW | milli Watts |
| GHz | Giga Hertz |
| cm | Centimeter |
| μm | Micrometer |
| sccm | standard cubic centimeter per minute |
| mTorr | milli-Torr (of pressure) |
| ml | milli-liter (of fluid) |

NOTATION

| | |
|------------------------------------|--|
| W | Rib width [μm] |
| H | Rib height [μm] |
| h | Slab height [μm] |
| r | $\frac{h}{H}$ ratio |
| n | Refractive index |
| n_{eff} | Effective refractive index |
| n_g | Group refractive index |
| λ | Wavelength |
| β | Propagation constant |
| ϕ | Phase of the EM wave |
| R | Waveguide bending radius |
| L | Length (refers to device length, component length) |
| L_{mmi} | length in MMI coupler for 3-dB splitting |
| W_{mmi} | Width in MMI coupler |
| κ | Coupling coefficient or strength of coupling |
| δ_{ch-ex} | Channel extinction |
| $\Delta\lambda$ | Channel spacing |
| ω_x | Electric field distribution in horizontal direction (along x-axis) |
| ω_y | Electric field distribution in vertical direction (along y-axis) |

CHAPTER 1

Introduction

In this introductory chapter, we first discuss about the motivation in carrying out the research investigation on integrated optical Mach-Zehnder interferometer (MZI) in silicon-on-insulator (SOI) platform. Afterwards, the major objectives of this work have been discussed in brief. Finally, the organization of entire thesis has been outlined.

1.1 Motivation

The advancement of SOI based CMOS technology has led to reduction in size of transistors and thereby increasing both speed and on-chip device density. This has ensured Moore's law to be valid even today. However, various studies show that increased interconnect delay due to various fringing effects is a major limiting factor for over-all performance [1, 2]. This has been explained nicely using the plot shown in Fig. 1.1 [3]. The black line in the plot represents the gate delay, which is monotonically decreasing as the technology node moves towards 100 nm. This reduction in gate delay translates into improvement in speed of the transistor. The dashed pink line, shows Aluminum (Al) interconnect delay. The sum of Al & SiO₂ based interconnect delay and gate delay is represented by pink line, which shows that beyond 250 nm technology node the total delay increases with the advancement of technology. This is because, scaling of interconnects leads to increase in resistance (R) and capacitance (C) between the metal lines as the technology node reduces. In order to improve the conductivity of the interconnects, researchers have replaced Al with Copper (Cu), which has higher conductivity and SiO₂ with Low-K dielectric, for isolation between the metal lines to reduce the capacitance which has in turn reduced the interconnect delay slightly (dashed blue). However, beyond 180 nm technology node even with Cu & Low-K dielectric based interconnect, the total delay has surpassed the gate delay and hence cannot be used to achieve high speed devices [2]. This bottle-neck of interconnect delay has been a hot area of research during past decades [4, 5]. Many R&D labs including semiconductor giants like

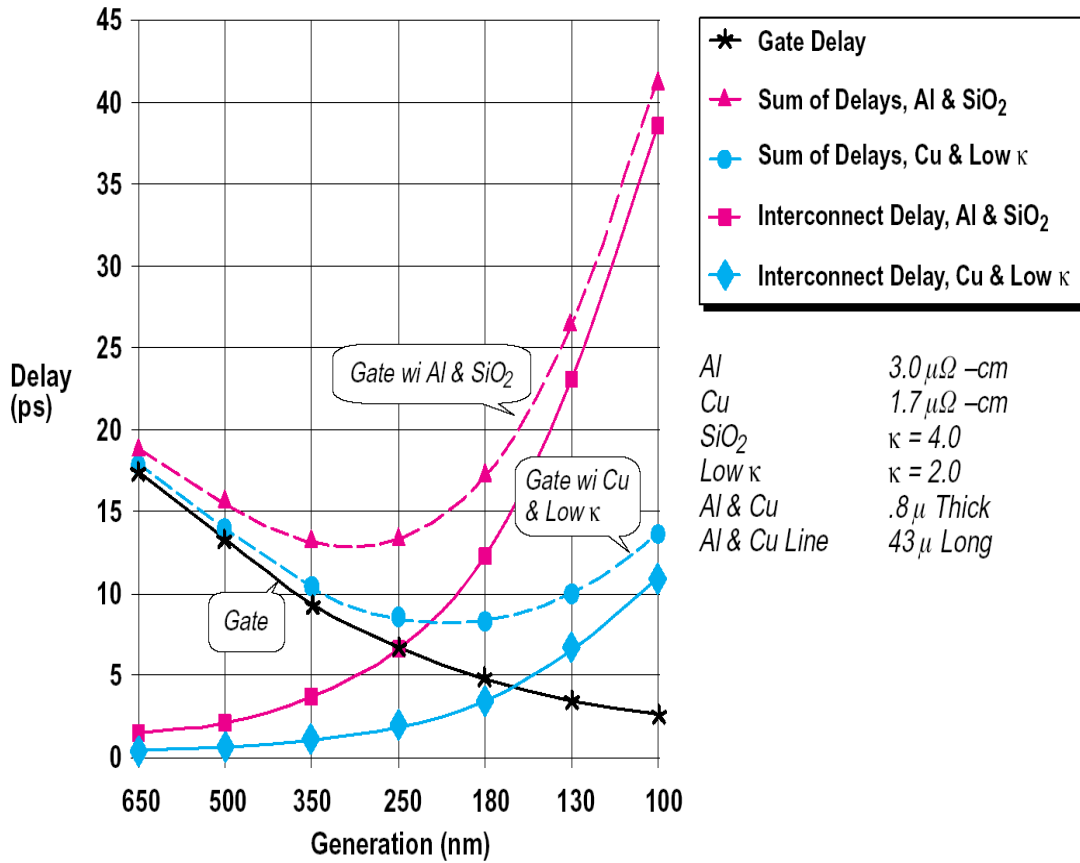


Figure 1.1: Various interconnect delays with the advancement towards higher technological nodes [3]

IBM and Intel have been actively engaged in developing CMOS compatible high-speed photonic devices in SOI platform in order to replace electrical interconnect with the broadband optical interconnect [6, 7, 8]. Devices such as Raman lasers [14, 15], Si-Ge photo-detectors [16, 17, 18], modulators [19], ring-resonators [20, 21], grating couplers, star couplers [22, 23], switches [24, 25], add/drop multiplexers [26, 27] etc., have been demonstrated in SOI platform by various groups. There is a world-wide attention to optimize the design and fabrication of above mentioned components/devices to be integrated with CMOS electronics.

The IBM Inc. has recently proposed a solution to overcome interconnect bottle-neck using 3-D Processor by making use of optical interconnects as an alternative to copper interconnects [9]. Incorporation of optical interconnects could solve many physical problems of interconnects and provide precise clock distribution, system synchronization, improved bandwidth and reduction in power dissipation [2, 4].

The proposed architecture of 3-D processor is shown in Fig. 1.2: the bottom layer

is the processor layer that consists of processor cores over which the memory layer is present, above the memory layer there is a photonics layer which consists of modulators, switches, WDMs and photo-detectors used for core to core communication. Communication between two different cores (say Core 1 to Core N) in such a processor takes place as follows : At the transmitter-end, data from Core 1 is passed through a serializer which converts serial data into parallel data, each of this parallel data is given to a CMOS driver which generates a voltage signal to modulate the light coming from an off-chip laser source. The modulated channels are then multiplexed using wavelength division multiplexer (WDM) and the switches route the signal to its designated paths. At the receiver end there is a de-multiplexer whose output is detected using an on-chip photo-detector, the current from the detector is given to CMOS amplifier. This amplifier output is then given to the CMOS serializer where the data is converted into the serial data and given to the core N of the processor.

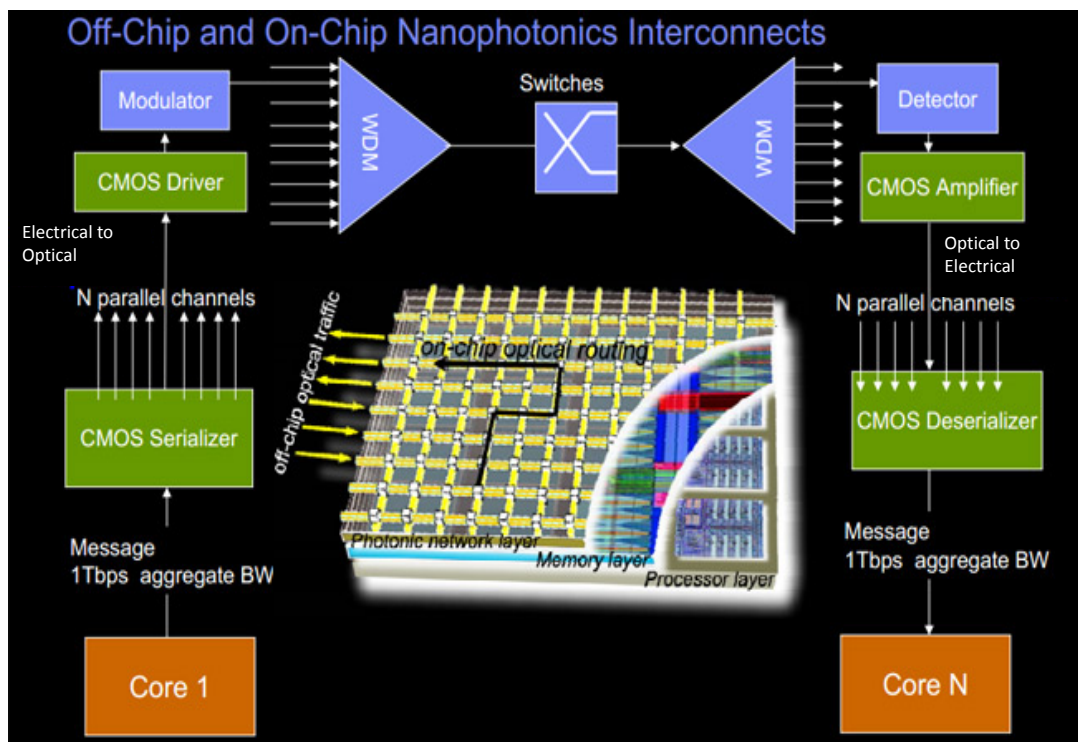


Figure 1.2: IBM proposal of 3-D processor using optical interconnects [9].

Silicon-on-insulator is found to be an excellent platform for optical interconnects because of the following reasons :

- Silicon is transparent at telecommunication wavelengths ($\lambda \sim 1.55\mu\text{m}$) [10].
- Higher refractive index contrast in SOI results tighter confinement, there by allowing compact structures with sharp bends [11].
- Electro-optic and Thermo-optic tuning in silicon allows demonstration of active devices.
- Commercial availability of optical grade wafer allows fabrication of photonic devices with low-loss [12].
- Well established CMOS fabrication technology can be used to fabricate photonic devices [11, 13].

Very recently, IBM inc. in connection to their proposed 3-D processor, has demonstrated a silicon nanophotonic chip [13] which consists of CMOS electronics and photonics devices integrated on same chip. Modulator, Si-Ge photo-detector, gratings and WDM filters along with cascaded amplifiers are integrated on SOI platform using 90-nm CMOS technology. The 4-channel WDM filter having a number of cascaded asymmetric Mach-Zehnder Interferometer (MZI) is shown in Fig. 1.3 (a). Top-view of a single asymmetric directional coupler (DC) based MZI present on the nanophotonic chip is shown in Fig. 1.3 (b), where the blue lines represent the waveguides with metal lines (yellow) acting as an heater.

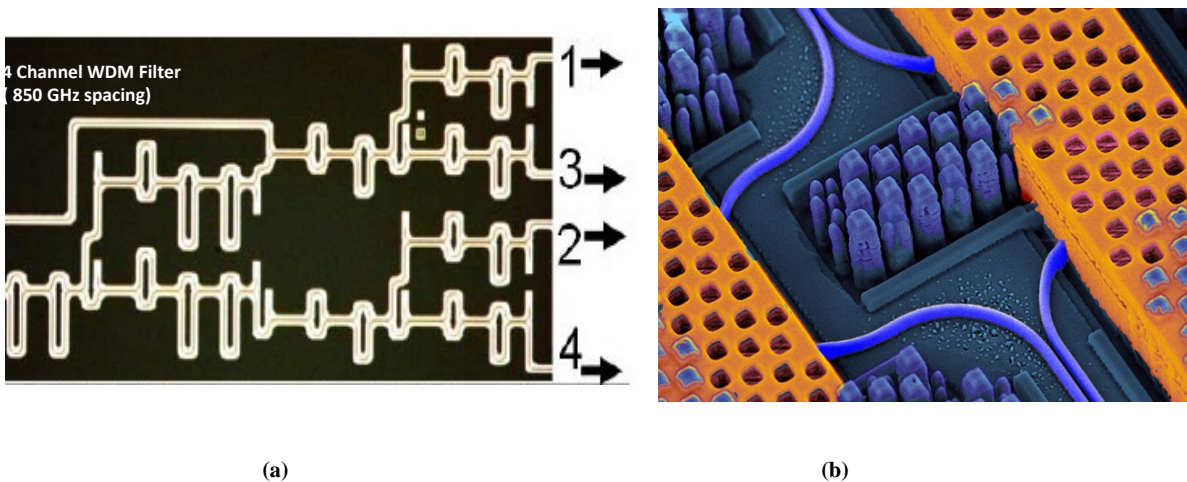


Figure 1.3: (a) Cascaded asymmetric MZIs used for 4-channel WDM filter in CMOS nanophotonic chip, (b) close view of a single asymmetric MZI (blue) along with resistive heaters (yellow) [13].

Besides WDM channel filter, MZIs are also used in add-drop multiplexers [26, 27] and high-speed modulators[28]. Hence, there is a need to demonstrate an compact, dis-

persion free and polarization independent MZI for DWDM applications. Our earlier studies here at IIT Madras show that, MZIs demonstrated with photonic wire (PhW) or photonic wire rib waveguides (PhWRW) are very compact in size, but are highly polarization dependent and also prone to waveguide dispersion[29]. Hence, PhW and PhWRW are not suitable for on-chip filtering applications over a wide range of wavelengths. We have previously demonstrated an MZI using large cross-section rib waveguides (LCRW), where the device layer is $\sim 5 \mu\text{m}$, which showed a nearly dispersion free response. However, because of the large waveguide dimensions the foot-print of the device increases(3 *cms*), such an MZI based interleaver may be useful for off-chip filtering applications but un-suitable for cascading two or more interleavers for on-chip filtering applications.

Recently it was observed that reduced cross-section rib waveguide structures (RCRW), with device layer thickness of $\sim 2 \mu\text{m}$, are compact relative to LCRW structures and provide nearly dispersion-free characteristics, which is useful in filtering applications [30]. Moreover, by carefully designing the dimensions of the waveguide; polarization independent waveguides can be achieved [31]. Some of the devices demonstrated with RCRW are ring resonator [32], photo-detector [16], polarization splitter [33], multiplexer and de-multiplexer [30].

1.2 Research Objective

The major objective was to demonstrate a compact, dispersion-free and nearly polarization independent MZI structures in SOI platform with $\sim 2 \mu\text{m}$ device layer thickness. The entire research work is sub-divided as described below.

- Design of single-mode reduced cross section rib-waveguide (with device layer $\sim 2 \mu\text{m}$)
- Design of polarization and wavelength independent MMI based 3-dB coupler
- Optimizing various design parameters for realizing MMI based MZI for ITU channel interleaver.
- Fabrication and characterization of 2×2 MZI based Interleaver on SOI.

1.3 Thesis Organization

The entire thesis work has been discussed in five chapters. At first, the working principle of MZI, its theoretical analysis, various design parameters and related simulation results are discussed in Chapter 2. This is followed by mask design and device fabrication process in Chapter 3. The characterization results of MMI, MZI are presented in Chapter 4. Finally, the whole thesis work is summarized in Chapter 5.

CHAPTER 2

Design and Simulations

In this chapter we will discuss about design of a compact, dispersion free and nearly polarization independent MZI in SOI platform. Background theory has been discussed in Section 2.1. The basic building blocks of MZI i.e., single-mode waveguides and MMI couplers have been discussed in Sections 2.2 and 2.3, respectively. Finally, overall design and performance of an MZI has been presented in Section 2.4.

2.1 Background Theory

A schematic top view of an MZI with asymmetric arms has been shown in Fig. 2.1. It is a bidirectional device that has two input and two output ports. The signal power launched at one of the two input ports is equally split by the input 3-dB splitter and independently guided into two arms of the MZI. Depending on the phase relationship between the signal in two arms of the interferometric arms, they interfere at the second 3-dB coupler (which acts as a combiner) and accordingly the signal powers are distributed between Port 3 and Port 4, respectively.

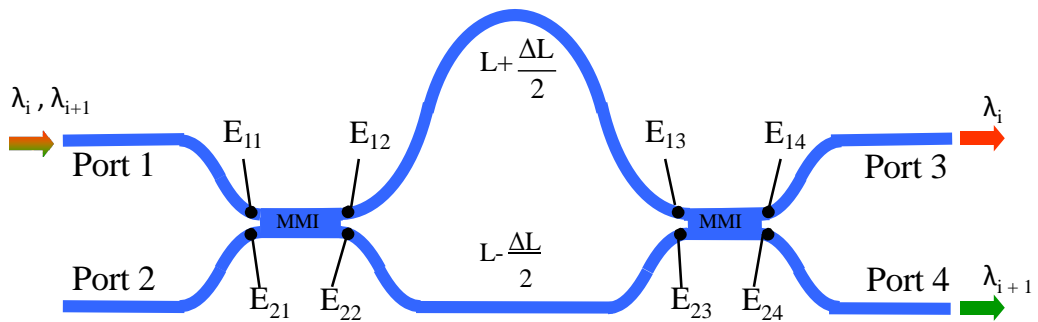


Figure 2.1: Schematic top view of an unbalanced MZI. Various symbols are used for mathematical modeling (see text).

The working principle of the MZI can be understood using transfer matrix approach [34]. As shown in Fig. 2.1, we have annotated the electric field amplitudes associated with the guided modes at different points in the device: E_{1i} (E_{2j}) are the electric fields at different locations in upper (lower) arm of the Mach-Zehnder Interferometer. The transfer matrices corresponding to the first 3-dB coupler, the unbalanced arms and the second 3-dB coupler can be written as:

$$\begin{bmatrix} E_{12} \\ E_{22} \end{bmatrix} = \begin{bmatrix} \frac{1}{\sqrt{2}} & -j\frac{1}{\sqrt{2}} \\ -j\frac{1}{\sqrt{2}} & \frac{1}{\sqrt{2}} \end{bmatrix} \cdot \begin{bmatrix} E_{11} \\ E_{21} \end{bmatrix} \quad (2.1)$$

$$\begin{bmatrix} E_{13} \\ E_{23} \end{bmatrix} = e^{-j\beta L} \begin{bmatrix} \exp(-j\phi) & 0 \\ 0 & \exp(j\phi) \end{bmatrix} \cdot \begin{bmatrix} E_{12} \\ E_{22} \end{bmatrix} \quad (2.2)$$

$$\begin{bmatrix} E_{14} \\ E_{24} \end{bmatrix} = \begin{bmatrix} \frac{1}{\sqrt{2}} & -j\frac{1}{\sqrt{2}} \\ -j\frac{1}{\sqrt{2}} & \frac{1}{\sqrt{2}} \end{bmatrix} \cdot \begin{bmatrix} E_{13} \\ E_{23} \end{bmatrix} \quad (2.3)$$

It has been assumed that the length of two arms of MZI between the MMI couplers are $L + \frac{\Delta L}{2}$ and $L - \frac{\Delta L}{2}$, respectively. It is also assumed that both the waveguides are single-mode guiding and identical, having propagation constants of $\beta = \frac{2\pi n_{eff}}{\lambda}$, where n_{eff} is the effective index of the guided mode at wavelength λ . Thus, the acquired phase difference due to the unbalanced arms of MZI is $\phi = \beta\Delta L$. Moreover, the 3-dB MMI coupler introduces a phase of $\frac{\pi}{2}$ at the cross port w.r.t the bar port of the 3-dB MMI coupler. When $E_{21} = 0$, it can be shown that the powers in Port 3 and Port 4 of MZI are proportional to $\cos^2 \phi$ and $\sin^2 \phi$, respectively (see Appendix A.1). Since ϕ is function of λ , the response of the device is a periodic function of wavelength in either ports. If $\beta_i\Delta L = (2m + 1)\pi$ and $\beta_{i+1}\Delta L = 2m\pi$ are satisfied (m , is an integer), an incoming wavelength λ_i would appear in Port 3 and neighboring channel λ_{i+1} would appear in Port 4, respectively. Therefore, to extend the design of MZI for interleaving applications with desired channel spacing ($\Delta\lambda = |\lambda_{i+1} - \lambda_i|$), ΔL serves as the main determining factor. The path length difference ΔL (see Appendix A.1 for derivation) between the two arms of the MZI can then be expressed as [35]:

$$\Delta L = \frac{c}{2n_g \Delta\nu} \quad (2.4)$$

where, $\Delta\nu = \frac{-c \cdot \Delta\lambda}{\lambda^2}$, and group index n_g is defined by

$$n_g = n_{eff} - \lambda \frac{dn_{eff}}{d\lambda} \quad (2.5)$$

It is evident from Eq. 2.4 that for designing Mach-Zehnder Interferometer to separate DWDM channels uniformly with desired channel spacing $\Delta\nu$, the required ΔL depends on the group refractive index (n_g) of the guided mode. Therefore, in order to obtain better device characteristics, dispersion-free waveguide structure (n_g is constant w.r.t wavelength) with single-mode guiding, accurate design of MMI couplers with wavelength independent 3-dB power splitting and low-loss s-bend waveguides are desired. Each of these will be discussed separately in following sections.

2.2 Single-mode Waveguide with 2- μm SOI

Typical cross-sectional view of a silicon rib waveguide has been shown in Fig. 2.2. Four different single-mode waveguides cross-sections namely photonic wire waveguide (PhWW), photonic wire rib waveguide (PhWRW), reduced cross-section rib waveguide (RCRW) and large cross-section rib waveguide (LCRW) were initially studied. The cross sectional geometries of these waveguide structures are obtained by scaling the waveguide width W , height H and slab height h in the structure shown in Fig. 2.2. The dimensions (see Table 2.1) were carefully chosen from the published literature's demonstrating various functional silicon photonic devices [36, 37, 38, 39].

Table 2.1: Classification of SOI waveguides based on cross-sectional dimension.

| Waveguide | Parameters [μm] | Reference |
|-----------|--------------------------------|-----------|
| PhWW | $W = 0.50, H = 0.22, h = 0.00$ | [38, 40] |
| PhWRW | $W = 0.50, H = 0.22, h = 0.05$ | [41, 42] |
| RCRW | $W = 1.30, H = 2.00, h = 0.84$ | [14, 36] |
| LCRW | $W = 5.00, H = 5.00, h = 3.20$ | [37, 39] |

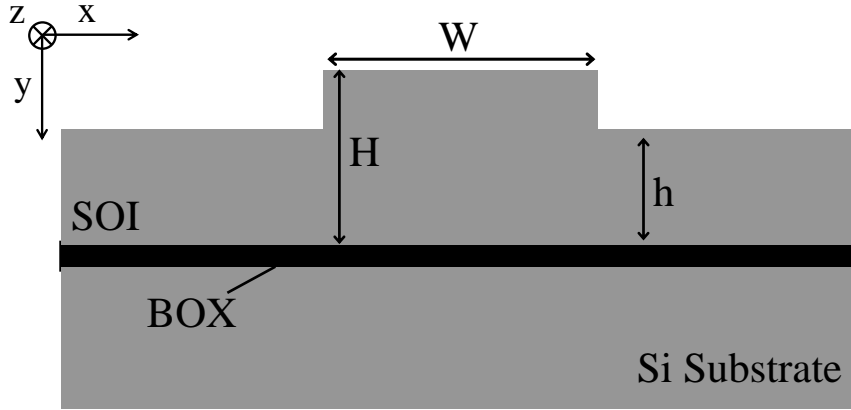


Figure 2.2: Schematic cross-sectional view of a typical silicon rib waveguide structure. The controlling parameters for single-mode guiding are waveguide width W , height H and slab height h . The bottom and top claddings are considered to be buried oxide (SiO_2) and air, respectively.

Wavelength dependent group index variation for guided fundamental modes have been presented in Fig. 2.3. Clearly, the photonic wire waveguide structures are highly dispersive, while RCRW and LCRW are less dispersive. The group index dispersion $\left(\frac{dn_g}{d\lambda}\right)$ at $\lambda = 1550$ nm for TE polarizations are estimated to be -10^{-5} /nm and -3.5×10^{-6} /nm for RCRW and LCRW, respectively (see Table 2.2). These calculations were carried out considering material dispersion characteristics of silicon using Sellmeir's coefficients [43]. The group index variation for bulk silicon is -3×10^{-6} /nm, clearly suggesting that the waveguide dispersion is negligible for LCRW structures and total dispersion is dominated by material properties of silicon. It is worth to mention here that the group index dispersion's for TM polarization also show a similar trend for all four waveguide geometries. Moreover, the waveguide birefringence of SOI based structures can result in different values of ΔL for TE and TM polarizations, and consequently affect the device response. Calculated waveguide birefringence ($n_{eff}^{TE} - n_{eff}^{TM}$) and guided fundamental mode sizes for TE polarization are given in Table 2.2. Clearly, the sub-micron structures are strongly polarization dependent while the RCRW and LCRW structures are relatively less polarization sensitive.

Hence, initially LCRW structures were used to demonstrate the DWDM channel Mach-Zehnder Interferometer. However, because of the large waveguide dimensions, the foot-print of the device was large (~ 3 cms). This makes the device difficult to cas-

cade with other structure. Therefore, RCRW structures were taken up as an alternative to the LCRW in order to design a compact MZI structure for filtering applications.

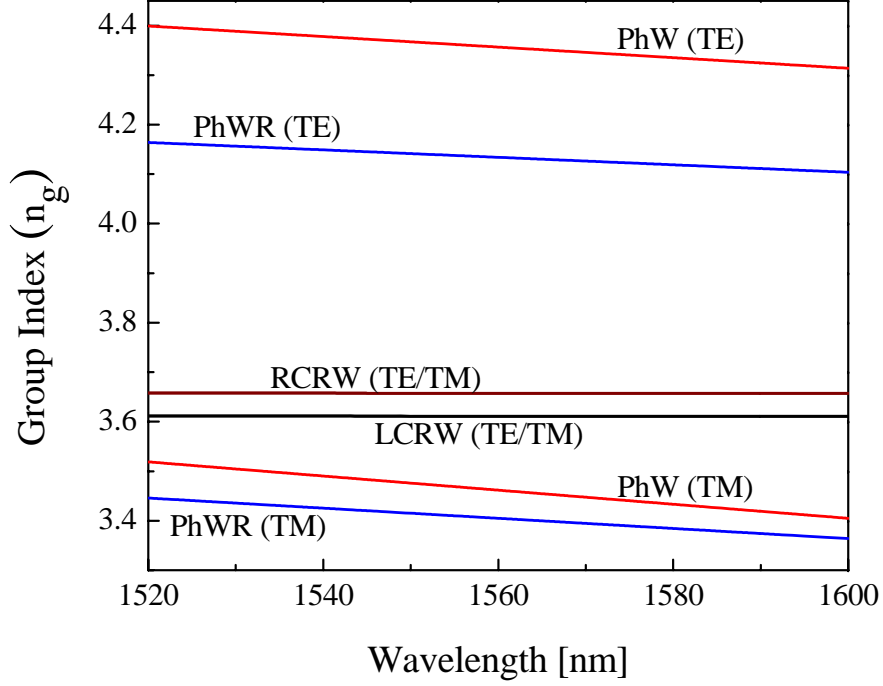


Figure 2.3: Group index as a function of wavelength for various single-mode waveguide structures in SOI platform [29].

Table 2.2: Group index dispersion slopes, waveguide birefringence and, mode-size for various waveguide structures at $\lambda = 1550$ nm.

| Waveguide | $\left(\frac{dn_g}{d\lambda}\right)$ [nm ⁻¹], (TE) | $n_{eff}^{TE} - n_{eff}^{TM}$ | Mode-size [$\mu\text{m} \times \mu\text{m}$], (TE) |
|-----------|---|-------------------------------|---|
| PhWW | -9.48×10^{-4} | 0.7 | 0.30×0.22 |
| PhWRW | -6.38×10^{-4} | 0.8 | 0.32×0.22 |
| RCRW | -2.27×10^{-5} | -6×10^{-6} | 1.3×1.5 |
| LCRW | -3.48×10^{-6} | -2×10^{-4} | 6.2×4.2 |

Earlier, the waveguide dimensions for RCRW structures ($W = 1.3 \mu\text{m}$, $H = 2 \mu\text{m}$ and $h = 0.84 \mu\text{m}$) was chosen after numerous simulations for zero-birefringence using mode-solver [29]. The birefringence at this dimension was found to be highly fabrication-sensitive. Hence, we re-designed the waveguide dimensions ($H = 2 \mu\text{m}$) using mode-solver. Single-mode condition of waveguide with $H = 2 \mu\text{m}$, for both the polarizations as a function of waveguide width (W) and slab height (h) is shown in Fig. 2.4

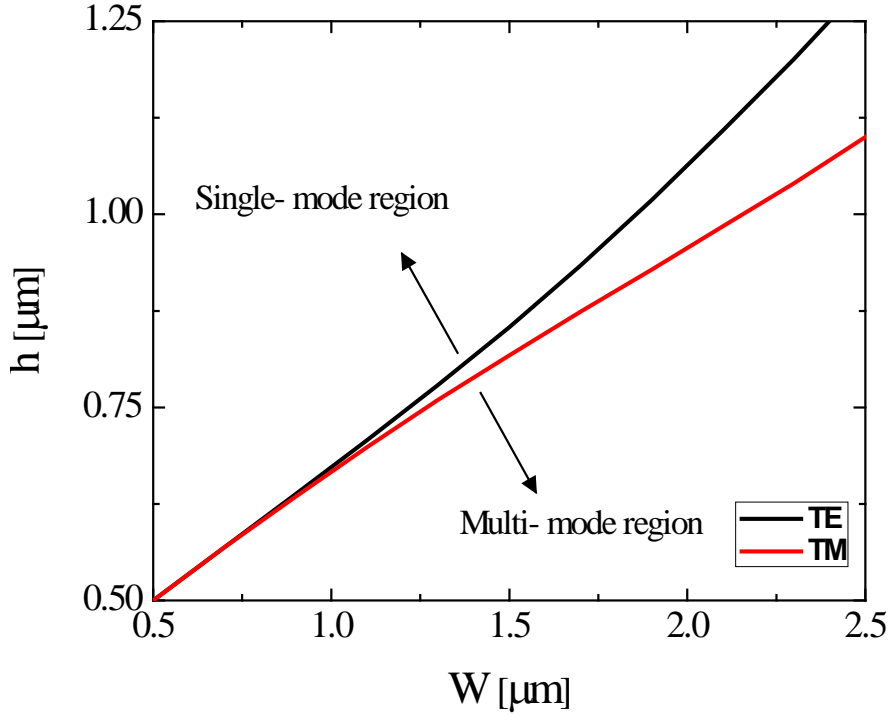


Figure 2.4: Single-mode region in W-h plane for RCRW in SOI for $H = 2 \mu\text{m}$ at $\lambda \sim 1550 \text{ nm}$, where W is the width of the rib waveguide and h is the slab height as shown in Fig. 2.2.

However, the commercially procured SOI wafer ($H = 2 \mu\text{m}$) usually has variations in device layer thickness (i.e., $H = 2 \pm 0.5 \mu\text{m}$). This variations in device layer thickness will result in birefringence change, which affects the device performance significantly. We have optimized the waveguide dimension, to make the device tolerant to such variations in device layer thickness. We have computed the birefringence for different device layer thickness i.e., $H = 1.6 \mu\text{m}$ to $H = 2.4 \mu\text{m}$ as a function of width (W) for a fixed value of $r = 0.5$ which is shown in Fig. 2.5. This plot allows us to choose a value of width (W), such that the variations in device layer thickness will have negligible effect on the birefringence of the waveguide.

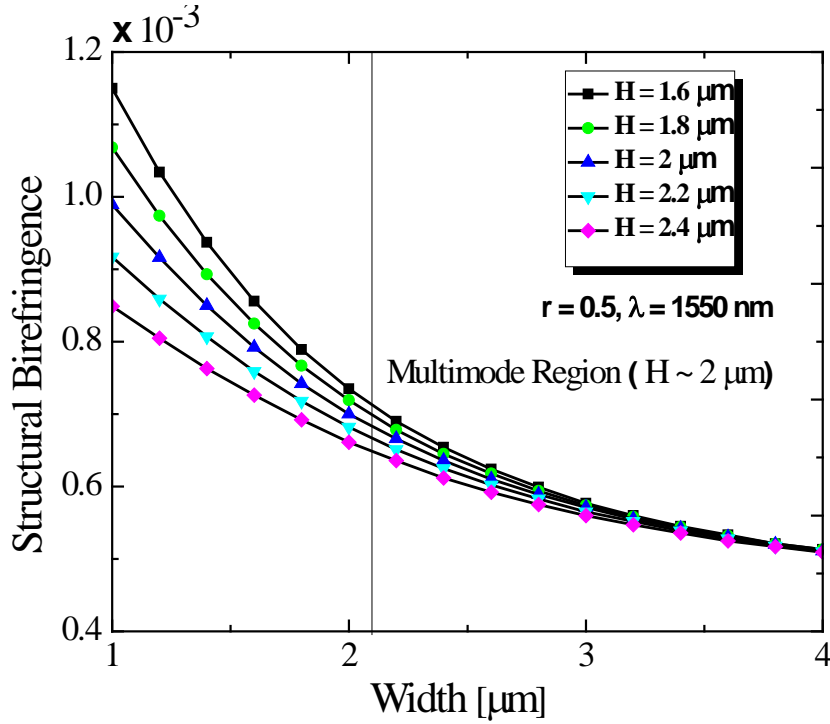


Figure 2.5: Structural birefringence ($n_{eff}^{TE} - n_{eff}^{TM}$) as a function of waveguide width for various device layer thicknesses with $(h/H) = 0.5$ at a wavelength of 1550 nm.

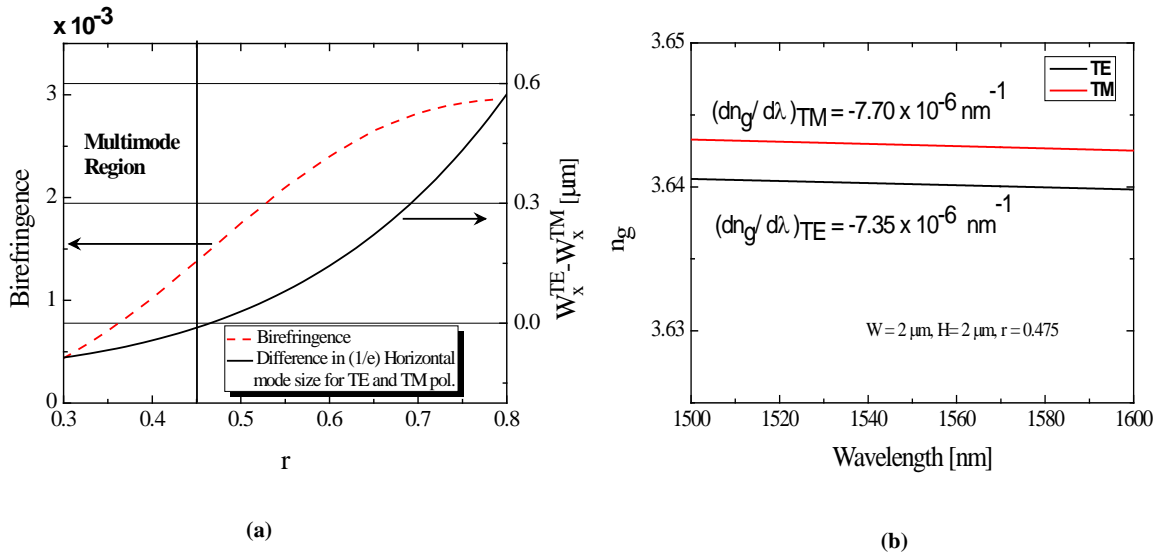


Figure 2.6: (a) Birefringence and difference in waveguide mode-size ($1/e$ horizontal spread at $\lambda \sim 1550$ nm) for two different polarizations as a function of $r = (h/H)$ for a device layer thickness of $2 \mu\text{m}$, (b) group index as a function of wavelength for the optimized waveguide parameters ($H = 2 \mu\text{m}$, $W = 2 \mu\text{m}$ and $r = 0.475$) for both polarizations of guided mode.

It was observed that, as the device layer thickness increases (for fixed W) the birefringence reduces (see Fig. 2.5). Also, as the waveguide width increases (for fixed H) the birefringence was reducing. This shows that larger dimension of waveguide leads to relatively lower birefringence. Moreover, the change in birefringence for different H (at given W) was decreasing as a function of width (W). Hence, in order to maximize the thickness dependent tolerance in birefringence, the waveguide width should be as large as possible. The difference in birefringence value, at single-mode cutoff ($W \sim 2 \mu\text{m}$) is found to be in the order of $\sim 10^{-5}$, for a variation in device layer thickness of $\Delta H = \pm 0.4 \mu\text{m}$ (at $H = 2 \mu\text{m}$).

Next, we try to optimize a value of $r (= \frac{h}{H})$, an important parameter in the design of single-mode rib waveguide. While designing our waveguide we select the value of r , in order to obtain identical guided mode-size, and there by achieving identical coupling/scattering losses for TE and TM polarizations, respectively. We have plotted birefringence & horizontal mode-size difference for both polarizations (see Fig. 2.6(a)) as a function of r . The difference in horizontal mode-size for both polarizations (see from Fig. 2.6(a)) is nearly zero at $r = 0.475$. Using waveguide parameters as $H = W = 2 \mu\text{m}$ and $r = 0.475$, group-index (n_g) for a wavelength range of 1500 nm to 1600 nm was calculated for both polarizations and plotted in Fig. 2.6(b). It can be seen that group index for both polarizations is nearly equal and almost constant ; this is essential to ensure a dispersion-free response of an MZI as Interleaver over a broad range of wavelengths.

2.3 MMI based 3-dB Power Splitter

As mentioned in Section 2.1, the proposed Mach-Zehnder structure has two identical couplers (3-dB power splitters). A power splitter or 3-dB coupler is an essential component of the MZI. While designing a 3-dB coupler we must ensure that the device satisfies the following requirements

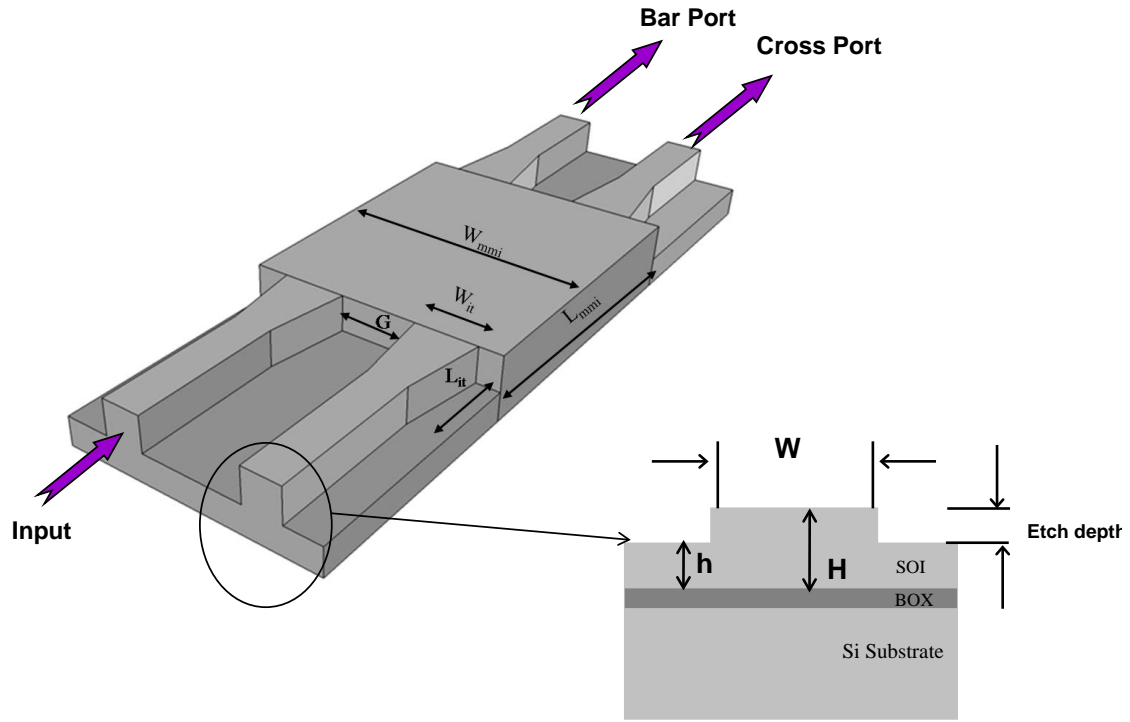
- Compact size
- Tolerant to fabrication errors
- Broadband and Polarization independent response.

One can use either a directional coupler (DC) based or multi-mode interference (MMI) based 3-dB splitter for MZI operation. Our simulations show that DC based 3-dB coupler is relatively longer, having low fabrication tolerance as well as polarization and wavelength dependent [29], which will not allow us to design a compact MZI for broadband operation. Whereas, MMI based 3-dB couplers are found to be more compact, fabrication tolerant as well as polarization and wavelength independent.

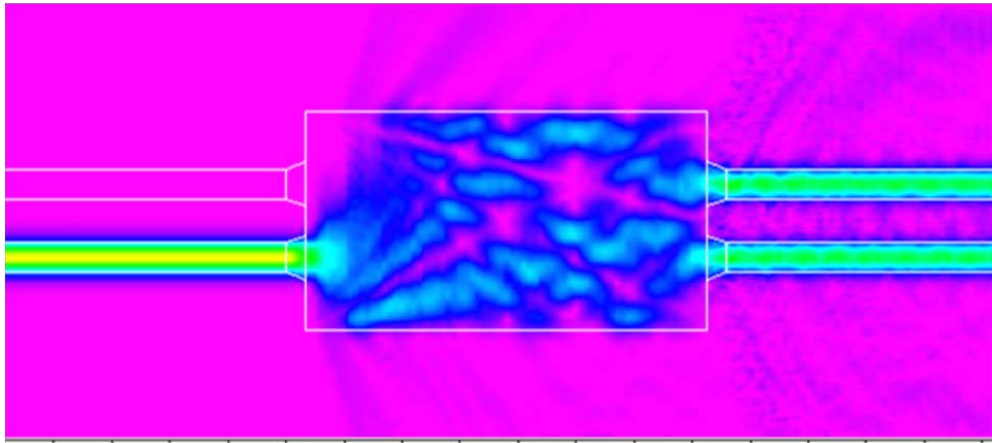
The optimization of MMI coupler was carried out using R-Soft beam propagation method (BPM) tool [44]. A schematic diagram of 2×2 MMI coupler, and the BPM simulation for power splitting characteristics of MMI coupler have been shown in Fig. 2.7. We have considered the excitation of symmetric modes for our MMI coupler by placing the inputs at $\pm \frac{W_{mmi}}{6}$ from the center of the MMI region, in order to achieve a compact structure [45]. The waveguide dimensions of $W = 2 \mu\text{m}$, $H = 2 \mu\text{m}$, $r = 0.475$ and a gap (G) = $2 \mu\text{m}$ between the input and output taper waveguides of the MMI coupler were chosen in our MMI design. The width of MMI structure was fixed at $W_{mmi} = 15 \mu\text{m}$, to accommodate tapering lengths and separation of input/output waveguides.

Optimization of MMI coupler was carried in following sequence:

- Keeping the input/output taper width fixed at $2 \mu\text{m}$, simulation was carried out to find the length of MMI region (L_{mmi}), where we get two distinct spots. The value of L_{mmi} was found to be about $354 \mu\text{m}$ from the first simulation.
- Fixing $L_{mmi} = 354 \mu\text{m}$, we varied the input taper width from $2 \mu\text{m}$ to $4 \mu\text{m}$ keeping the input/output taper length (L_{it}) at $15 \mu\text{m}$. By introducing the taper, the output power of MMI at both ports was gradually increasing up to a maximum value and then reducing beyond certain value W_{mmi} , as shown in Fig. 2.8(a). We fixed the input taper width (W_{it}) as $3 \mu\text{m}$, as it is the smallest width providing nearly uniform power in both ports.
- Using the above values of W_{it} and L_{mmi} , we varied the taper length L_{it} from $8 \mu\text{m}$ to $24 \mu\text{m}$ and found that the power was uniform and maximum at $L_{it} = 18 \mu\text{m}$.
- Using the above mentioned value of L_{it} , we re-ran the simulation by varying L_{mmi} from $334 \mu\text{m}$ to $364 \mu\text{m}$ in order to fine tune the image positions at the output of MMI region. We can see from Fig. 2.8(b) that as length of the MMI changes, the power in two output ports varies depending on the interference of excited modes in MMI; the power at two output ports as a function of L_{mmi} do not match - however at $L_{mmi} = 346 \mu\text{m}$ the powers in both ports was equal.



(a)



(b)

Figure 2.7: (a) Schematic 3-D view of 2×2 MMI coupler. Inset: cross-sectional view of SOI rib waveguide showing width W , height H and slab-height h , (b) BPM simulation showing power splitting characteristics of an MMI structure with optimized design parameters showing 3-dB power splitting at $\lambda = 1550$ nm for TE-polarization. - W_{mmi} is width of MMI region, L_{mmi} is the length of the MMI region, W_{it} is the width of the taper, L_{it} is the length of taper and G is the gap between access waveguides of MMI at input and output side.

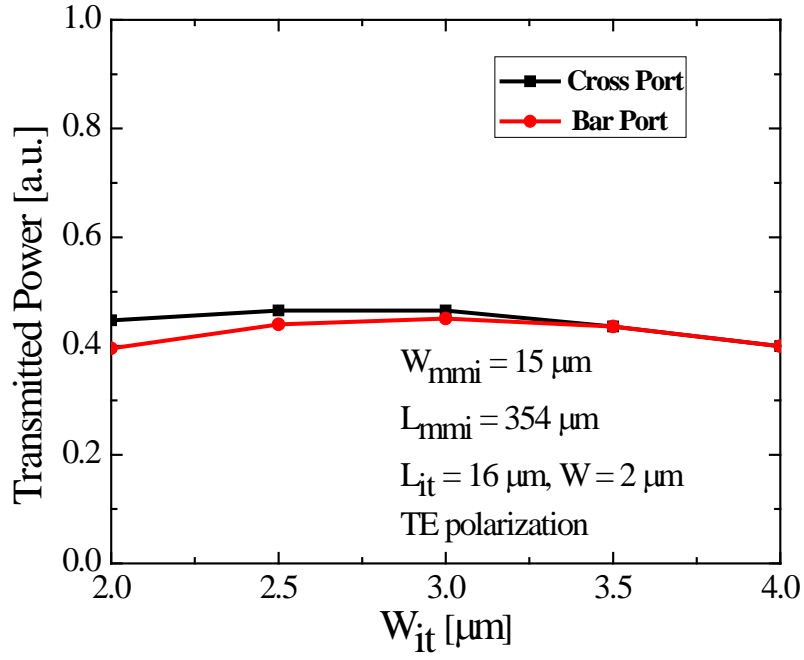
- Now we again varied L_{it} from 10 μm to 20 μm , and found that for $L_{it} = 14 \mu\text{m}$, the power at both ports are maximum and nearly equal with an insertion loss of 0.16 dB (for TE pol.) & 0.13 dB (for TM pol.).

The polarization and wavelength dependent splitting ratio of our optimized MMI splitter are shown in the Fig. 2.9(a). Splitting ratio is defined as fraction of power in bar port (or cross port) to the total transmitted power in both the output ports (bar port and cross port). For our optimized MMI splitter the splitting ratio is found to be nearly uniform for both polarizations over a wavelength range of 1500 nm to 1600 nm. The transmitted power as a function of r (within the range of single-mode guiding) for each port shows almost no variation for either polarizations (see Fig. 2.9(b)). This in turn improves the fabrication tolerance of proposed MMI based MZI structures.

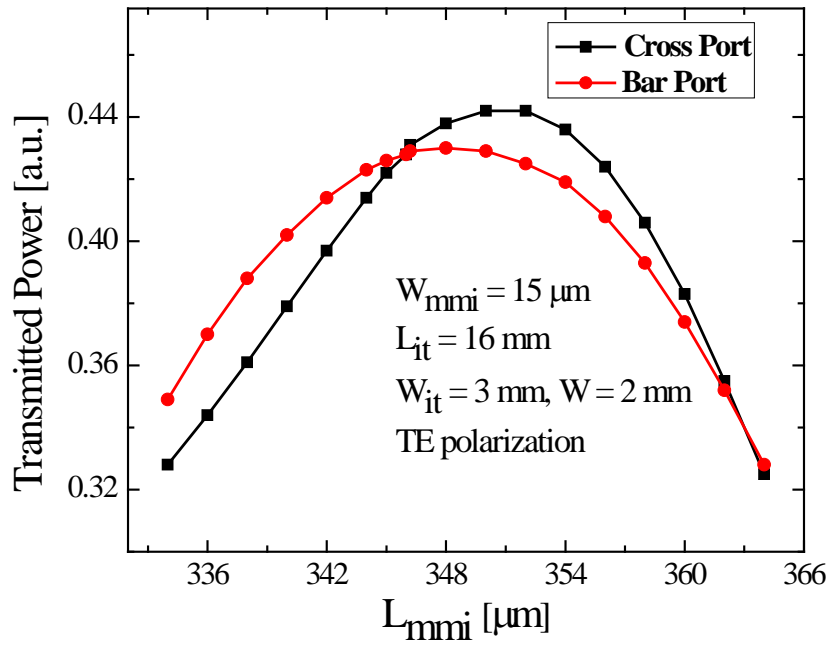
2.4 MMI Based 2×2 MZI Structure

Using the nearly polarization & wavelength independent design of MMI coupler we simulated a symmetric MZI, comprised of an input 2×2 MMI coupler (3-dB) followed by two identical straight waveguides (Length $L_{mzi} = 49 \mu\text{m}$) and an output 2×2 MMI coupler (3-dB) - so that the input power is transferred into the cross-port (port 4) (see in Fig. 2.10 (a)) and it is observed to be independent of the input polarizations and MZI length; Further the power could be switched into bar port by providing a π - phase shift in one of the MZI arms; this can be achieved either passively (by modifying waveguide parameters) or actively (by electro-optic or thermo-optic tuning). For example, by reducing the waveguide width ($W_m = 1.3 \mu\text{m}$) in one of the MZI arms, we could observe the input power to be switched completely into the bar port (port 3) for both the polarizations (see Fig. 2.10 (b)).

An incremental path length (ΔL) was added by introducing bends in one arm of the MZI section (see Fig. 2.11) in order to monitor the wavelength dependent performance of MZI as an interleaver. The value of differential path length $\Delta L = \frac{c}{2n_g \Delta \nu}$ is obtained from the transfer function of MZI [35]. In our MZI design the value of ΔL was chosen as $\sim 412 \mu\text{m}$ in order to separate alternate ITU channels in two output ports of MZI (to see it's performance as interleaver for 100 GHz channel spacing). for both

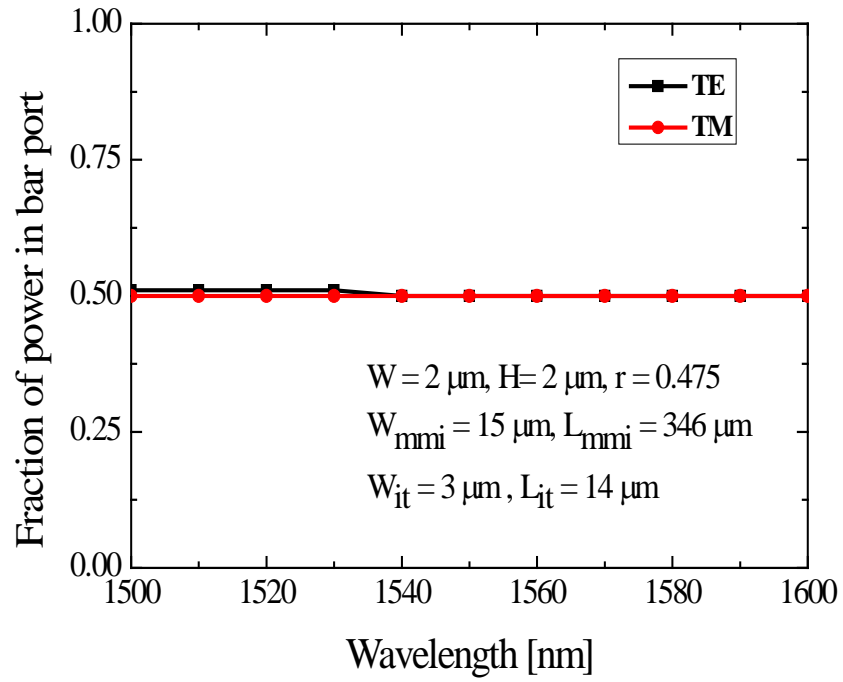


(a)

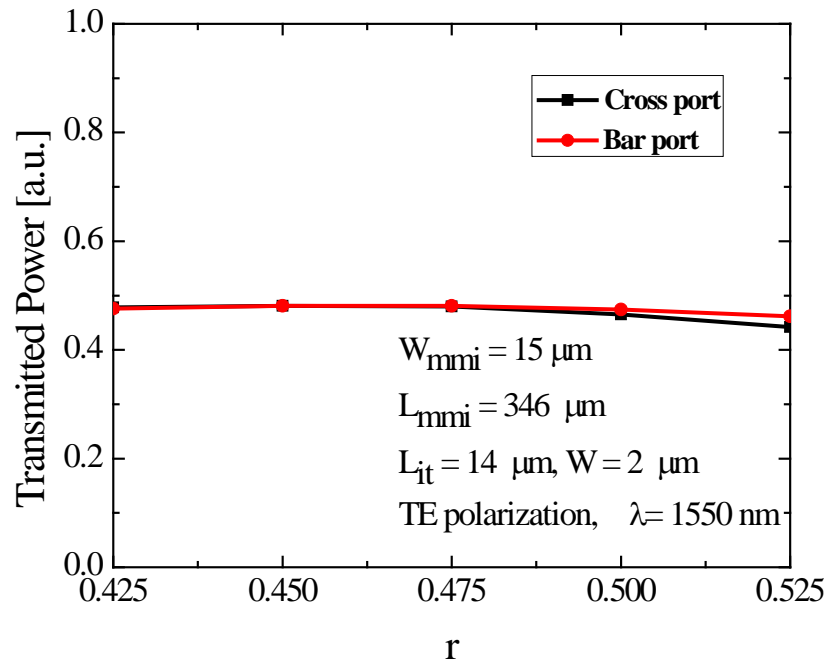


(b)

Figure 2.8: Transmitted powers in bar port and cross port of MMI based power-splitter as a function of (a) W_{it} and (b) L_{mmi}



(a)



(b)

Figure 2.9: (a) Polarization and wavelength dependent characteristics of optimized MMI based 3-dB power splitter, (b) transmitted power in bar port, cross port as a function of r for the optimized MMI based splitter.

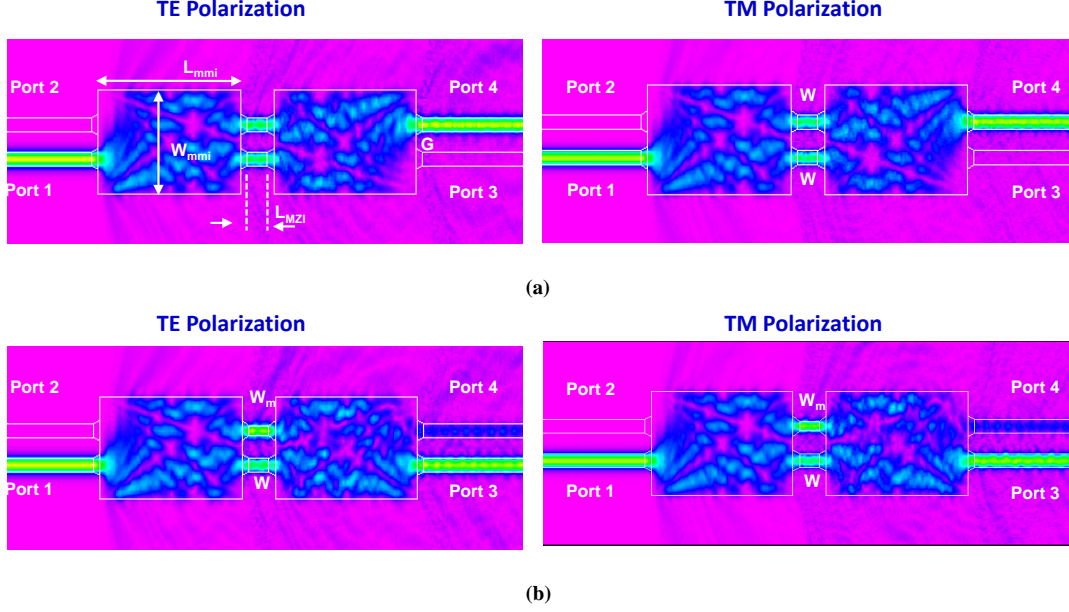


Figure 2.10: Simulated results of 2×2 MZI showing output only at the cross port for balanced arms (a), and only at the bar port for π -phase shifted unbalanced arms (b): W – waveguide width, W_m – width of asymmetric waveguide, W_{mmi} – width of the MMI region, L_{mmi} – length of the MMI region, W_{it} – width of the input and output access waveguides of the MMI, L_{it} – length of input taper, G – gap between the two input/output waveguides of the MMI, L_{mzi} – length of MZI arm for π - phase shift (see Table .2.3 for optimized design parameters).

polarizations. The schematic diagram of our asymmetric 2×2 MZI showing its various design parameters is shown in Fig. 2.11, and their optimized values are given in Table 2.3. The simulated transmission characteristics of the designed 2×2 asymmetric MZI shows an uniform inter channel extinction ratio at both output ports and is > 25 dB for a wide-band (1520 - 1600 nm) which is shown in Fig. 2.12. In our simulation, we have assumed that the waveguides are loss-less. However, scattering/insertion losses due to non-ideal adiabatic tapering and MMI junctions are inherently included in 3-D BPM simulator.

The response of the MZI at both the output ports as a function of wavelength is shown in Fig. 2.13(a). The simulated response shows a channel spacing of 0.8 nm (100 GHz) between bar and cross port and a 3-dB bandwidth of 100 GHz. Due to the slight polarization dependency of the single-mode RCRW structures. The simulated transmission characteristics of RCRW based interleaver show a polarization dependence. The polarization dependent response can be obtained using transmission matrix theory (see

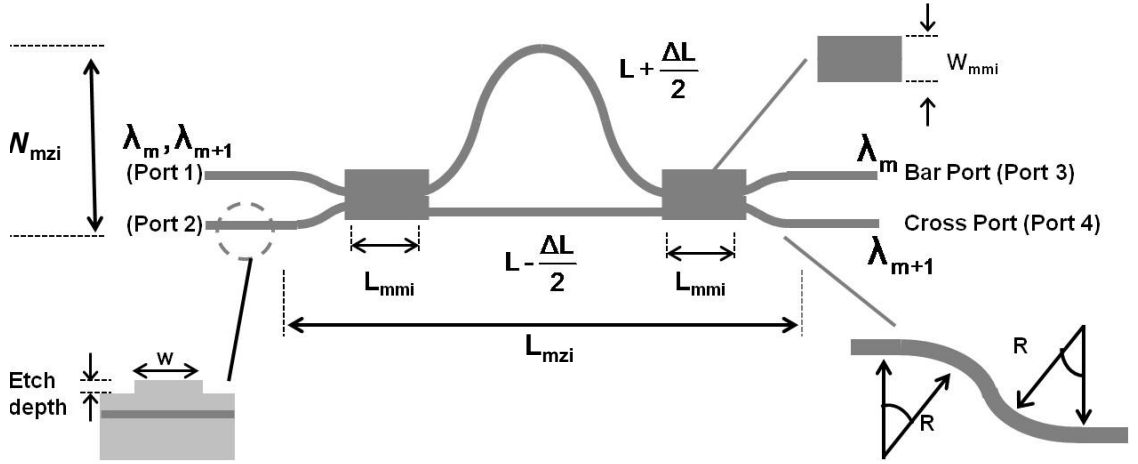


Figure 2.11: Schematic diagram of an 2×2 MZI based interleaver structure showing various design parameters of the MMI and waveguides W – waveguide width, W_{mmi} – width of MMI region, L_{mmi} – length of MMI region, L_{mzi} – length of MZI arm, R is radius of the bend waveguide, ΔL is the length of differential arm of interleaver. Inset: (a) cross-sectional view of SOI rib waveguide showing width W and etch depth, (b) top-view of bend used to separate the two MZI inputs/outputs where R – radius of the bend

Section 2.1) and incorporating the variation in effective index.

The Mach-Zehnder characteristics for single-mode RCRW based structure though dispersion-free are slightly polarization dependent as expected from the prior analysis. Wavelength dependent transmission characteristics of RCRW based MZI around $\lambda = 1550$ nm is shown in Fig. 2.13(b) for TE and TM polarization. The shift in resonance peaks at the two output ports for TE and TM polarization, is due to waveguide birefringence ($n_{eff}^{TE} - n_{eff}^{TM} \sim 10^{-3}$). It can be shown from Eq. 2.4, that waveguide birefringence affects the position of resonance peaks for different polarizations ($\delta\lambda = \lambda_r^{TE} - \lambda_r^{TM}$).

This shift in peak position can be tuned by controlling the waveguide dimensions or by incorporating active element such as a PIN modulator (for variable tuning) or heater element (for permanent tuning) in one of the arm of the MZI. Feasibility of incorporating such an element for correction in the peak position is being under study at our lab.

Bend waveguide structures are used in the asymmetric arm of the MZI to provide

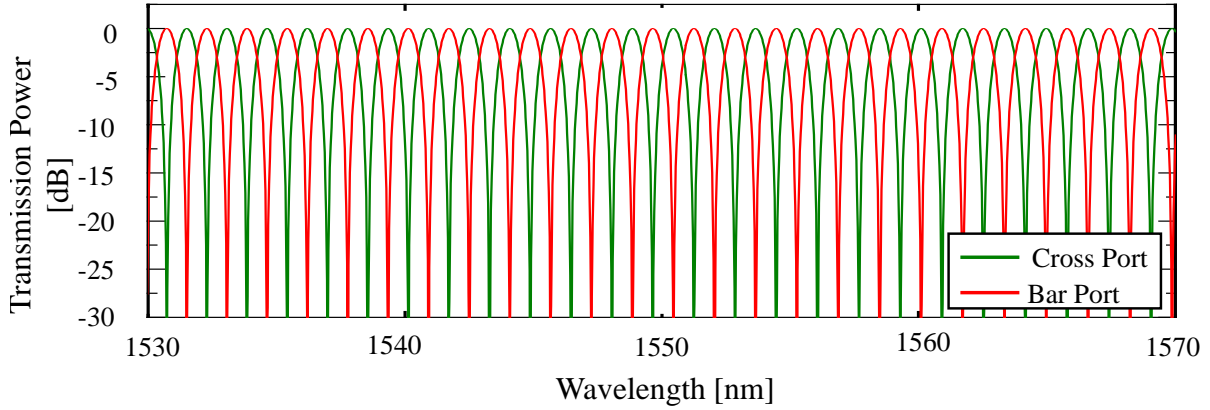


Figure 2.12: Simulated transmission characteristics at cross port and bar port of an un-balanced 2×2 MMI based MZI structure for TM polarization

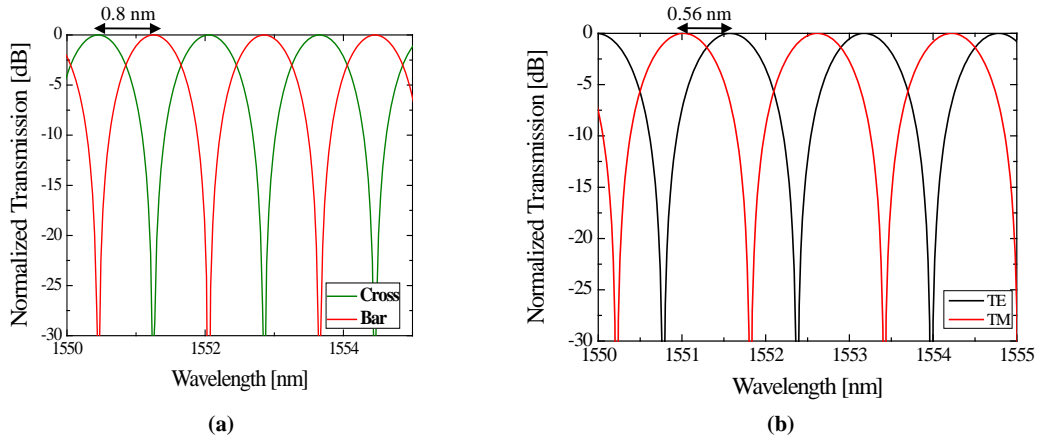


Figure 2.13: (a) Wavelength dependent characteristics for TM polarization and (b) Polarization dependent characteristics of an un-balanced 2×2 MMI based MZI structure

the differential path length as well as to separate the input and output waveguides in order to avoid launching of power into both ports at input and coupling at output ends. To fix the optimum value of bending radius we have calculated the bend loss of 90° bend waveguide (see Fig. 2.14), as a function of bending radius using Eigen mode solver [46].

Bend loss is a combination of mode mis-match loss between straight waveguide and bend region, and propagation loss in the bend region. However, the dominant factor is the mode mis-match loss, which is calculated by taking the overlap integral between computed mode profiles of the straight and the bend section. It is clear from the plot (see Fig. 2.14) that, as the radius of the bend increases the transmission loss decreases.

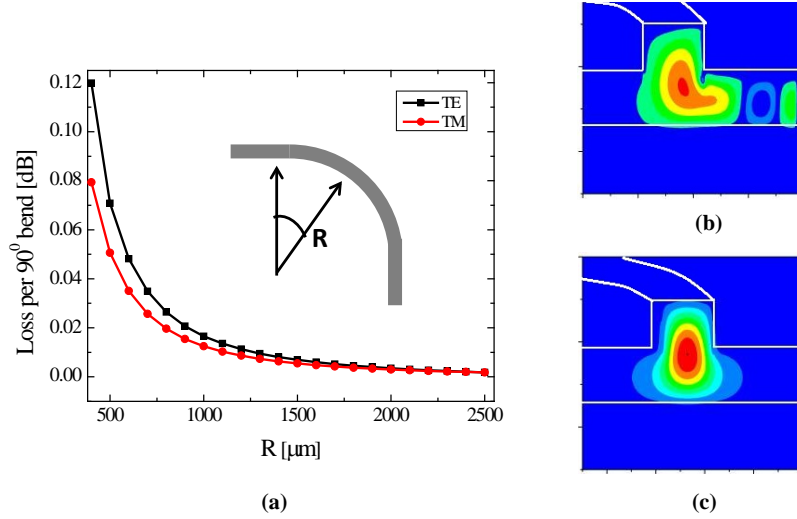


Figure 2.14: (a) Calculated transmission loss of a 90° bend waveguide structure (see Table 2.3 for waveguide parameters) as a function of bend radius for both TE and TM polarizations; (b) and (c) show the guided mode-field distributions for 100 μm , and 1000 μm bending radii, respectively for TE-pol.

Table 2.3: Optimized design parameters for single-mode waveguides, 3-dB MMI splitter and MZI based Interleaver structure

| | |
|---|------------------------------|
| $W = 2 \mu\text{m}$ | $W_{mmi} = 15 \mu\text{m}$ |
| $h = 0.95 \mu\text{m}$ | $L_{mmi} = 346 \mu\text{m}$ |
| Bending Radius (R) = 1000 μm | $\Delta L = 412 \mu\text{m}$ |
| Device Length = $\sim 5.2 \text{ mm}$ | Operation Band = C and L |

The bending radius of $R = 2 \text{ mm}$ or more provides almost loss-less bends. However, the dimension of the device increases. With $R \leq 1 \text{ mm}$, the design can be compact but at an expense of higher bend loss. In order to demonstrate a compact device we have chosen a bend radius of $R = 1000 \mu\text{m}$ in our design by compromising slightly on bend-loss. A typical mode-profile for a bend waveguide with radius of 0.1 mm (see Fig. 2.14(b)) is less confined and tend to leak into the slab region leading to higher bend waveguide loss, while the mode-profile for a bend waveguide with a radius of 1 mm (see Fig. 2.14(c)) is found to be well confined within the rib and hence provides low bend induced loss.

The final design of MZI (interleaver) is made by considering the above discussed and optimized waveguide parameters. The final design parameters are tabulated in Table 2.3. The MZI based Interleaver designed in this work is for interleaving ITU channels in 100 GHz DWDM grid, which was used while considering the design of ΔL using

Eq. 2.4. We have kept the output waveguides are kept $250 \mu\text{m}$ apart in order to allow efficient fiber pig-tailing of our device in future with standard SMF.

2.5 Conclusions

Theory and design of multi-mode interference based MZI has been discussed in this section . Dimensions for single-mode RCRW waveguides and MMI structure for polarization and wavelength independent splitting was optimized. Finally an MZI based interleaver structure on single-mode RCRW structures ($W = 2 \mu\text{m}$, $h = 0.95 \mu\text{m}$ and $H = 2 \mu\text{m}$) in SOI were designed, which resulted in a nearly dispersion-free response in the desired optical communication band (C+L). The MZI response was slightly polarization dependent (shift in peak position) which can be solved either by controlling the waveguide dimensions or by thermo/electro-optic tuning.

CHAPTER 3

Photomask and Device Fabrication

Using our optimized design parameters of RCRW single-mode waveguides, MMI splitter and MZI as discussed in Chapter 2, devices were fabricated for experimental investigations. Suitable masks were designed and fabricated for defining the device structures; details of which have been discussed in Section 3.1. The device fabrication steps have been presented in Section 3.2. Finally, experimentally obtained properties (losses and mode-profiles) of reference waveguides are presented in Section 3.3.

3.1 Mask Design and Fabrication

As mentioned in the previous chapter, the design parameters were chosen such that they can be defined/fabricated using conventional photolithography process. The mask layouts were designed using commercial R-soft CAD tool. A single module of mask consists of two Mach-Zehnder Interferometers, two straight waveguides, two meander bends and an MMI splitter which is shown in Fig. 3.1. Here, (Wg3, Wg4), (Wg7, Wg8) etc., form the MZIs, while the other reference structures are namely, meander-bend waveguides (Wg2, Wg9), MMI couplers (Wg5, Wg6), straight waveguides (Wg1, Wg10). These reference structures have been included to study various parameters like waveguide loss (straight waveguide), bend-induced losses, power splitting ratio and insertion loss (MMI coupler). There are three such sets (S1, S2, S3) in entire mask layout. These sets have MZI structures with same value of ΔL , but they differ by the length of MMI coupler ($L_{mmi} = 346 \mu\text{m}$, $353.5 \mu\text{m}$, and $361 \mu\text{m}$). The different lengths of MMI coupler (L_{mmi} , $L_{mmi} + \Delta L_{mmi}$, $L_{mmi} + 2\Delta L_{mmi}$), was chosen by taking into account the fabrication errors in width. The overall dimension of the mask layout is 2.5 cm (width) \times 2 cm (length).

The mask layout is transferred over a commercially acquired Cr coated ($\sim 50 \text{ nm}$) mask plate (4" \times 4" glass plate) having a thin layer ($\sim 540 \text{ nm}$) of photoresist (AZP-

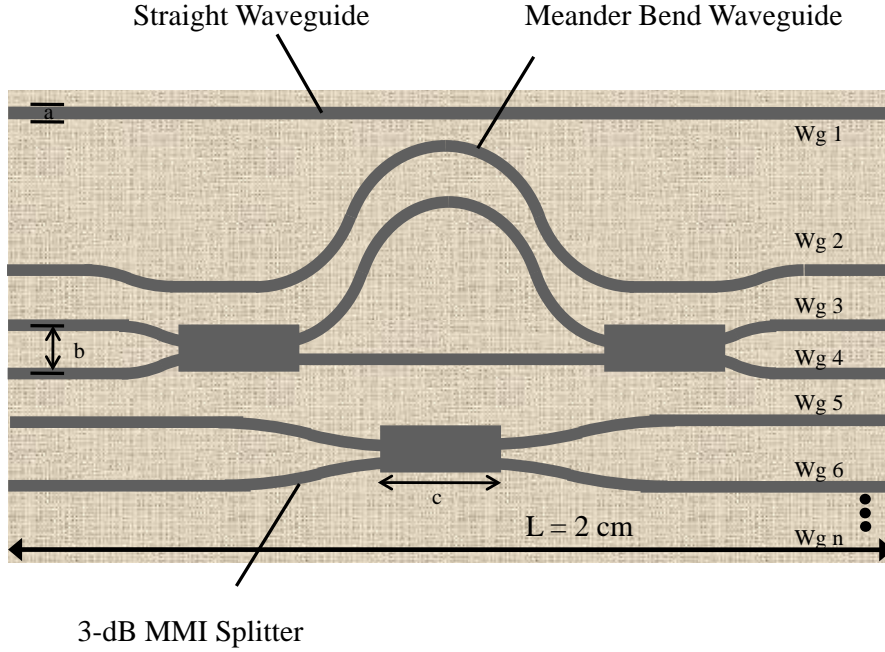


Figure 3.1: Schematic top view of one of the five sets in the interleaver mask. $a = 2 \mu\text{m}$, $b = 250 \mu\text{m}$ and $c = 346 \mu\text{m}$, $W_{set} = 2300 \mu\text{m}$ and $L = 2.8 \text{ cm}$.

1350). Pattern is directly written over the photoresist using UV laser writer (DWL - 66, Heidelberg Instruments GmbH, He-Cd laser source $\lambda = 442 \text{ nm}$). The exposed PPR is then developed using a 0.1 molar NaOH developer solution (7 pallets NaOH in 250 ml water). The photoresist pattern is later transferred to the Cr film using Ammonium Ceric Nitrate and Acetic Acid based etchant solution (see Appendix A.2). The undeveloped photoresist is finally removed by acetone cleaning.

3.2 Device Fabrication

The devices are fabricated on optical grade SOI wafers (Ultrasil Inc., USA). Detailed specifications of these wafers are listed below:

- Handle wafer thickness: $500 \mu\text{m} \pm 50 \mu\text{m}$
- Device layer thickness: $2 \mu\text{m} \pm 0.5 \mu\text{m}$
- Buried oxide thickness: $1 \mu\text{m}$
- Device layer resistivity: $> 5000 \Omega/\text{cm}$

- Crystal orientation: $\langle 100 \rangle$
- Wafer diameter: ~ 100 mm

Sequential device fabrication steps are: (i) wafer cleaning, (ii) photolithography for waveguide definition, (iii) reactive ion etching, and (iv) end-facet preparation. These fabrication process steps are schematically shown in Fig. 3.2. Each of these process steps have been discussed separately below. Towards the end of this section, a detailed summary of fabricated MZI samples is mentioned.

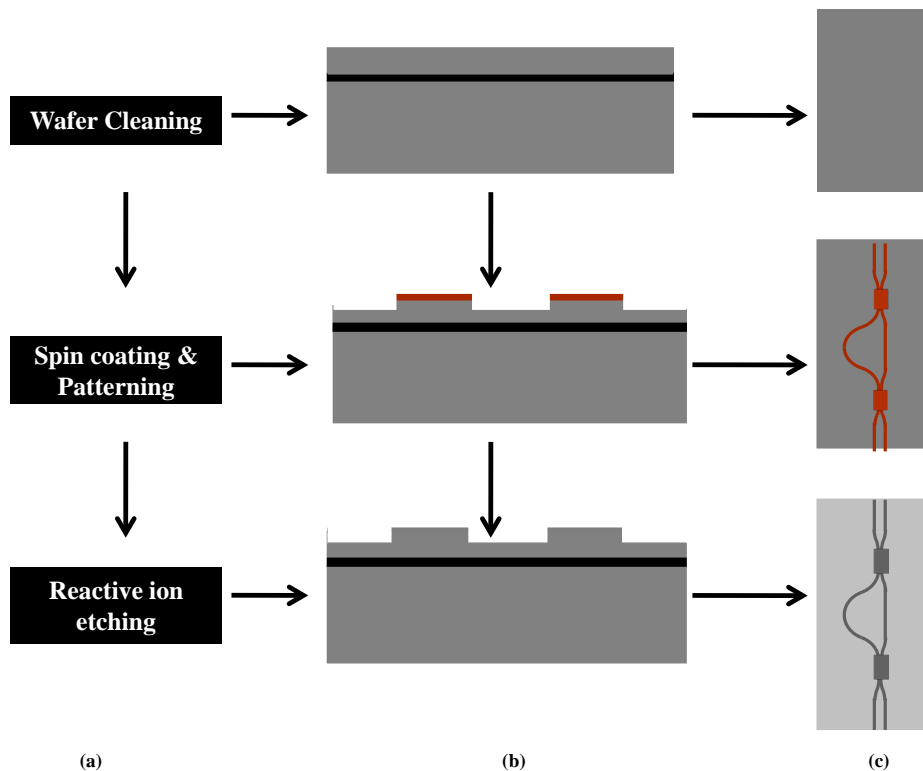


Figure 3.2: (a) Fabrication process steps, (b) Cross sectional view of of the sample SOI wafer, (c) Top section view of the sample SOI wafer.

(i) Wafer Cleaning

The SOI wafer with above mentioned specifications are diced/cleaved into smaller rectangular pieces (~ 1.5 cm \times 2 cm) to nearly accommodate the mask layout discussed in previous section as well as to fit to the dimension of sample-holder in our characterization setup. At first, samples are rigorously treated for removing any kind of organic/inorganic impurities. The organic impurities have been removed using trichloroethy-

lene (TCE) and acetone cleaning procedures, respectively. Wafer samples are immersed in TCE and the solvent is boiled (~ 55 °C) in a beaker for 2-5 min. Afterwards, the samples are cleaned by immersing them in acetone with ultrasonic agitation, followed by thorough rinsing with DI water. Later, the inorganic impurities are cleaned using conc. Nitric Acid (HNO_3). In this case, samples are immersed in HNO_3 and boiled at ~ 55 °C for 5 min. Cleaning with HNO_3 not only removes (dissolves) inorganic impurities but also grows a thin oxide layer (< 5 nm) on top of silicon wafer. The growth of oxide-film can be verified by hydrophilic nature of wafer surface. This oxide is removed by immersing the wafer in dil. HF solution (1:10 :: HF:H₂O) for ~ 30 s. Since the growth of oxide consumes silicon from the wafer, removal of oxide exposes a fresh wafer surface suited for fabrication of devices.

(iii) Photolithography

The mask pattern has been photolithographically transferred on the PPR-coated samples. At first, a thin layer (~ 1.5 μm) of positive photoresist (S1813-G) over sample surface is obtained using spin coating technique (spinning speed: 5000 rpm and, angular acceleration: 600 rpm/s). The positive photoresist (PPR) coated samples are then pre-baked at 80 °C for 17 min in an oven. This is done in order to harden the PPR layer as well as to evaporate humidity content and organic solvents.

The device mask is then aligned over the sample and exposed to 365 nm UV radiation (i-line) for ~ 13 sec using a 306 Watt UV lamp (Mask Aligner: BA6/MA6 Suss MicroTech). The exposure to UV radiation tends to break inter-molecular bonds of the photoresist, thereby making it soft to be removed using a NaOH based developer solution (0.1 molar NaOH). After exposure the sample is subjected to a post exposure bake at 120 °C for 5 to 10 minutes in an oven. This helps us to avoid over-developing of sample in developer solution. Typically, the optimized developing time is $\sim 38 - 40$ s at 25 °C temperature and, 50 % humidity for a sample exposed with UV intensity of 5.2 mW/cm². A sample was fabricated without post exposure bake resulted in over-developing of the device and showed a wavy nature (see in Fig.3.3) where as a sample with post exposure bake and optimized parameters gave nearly uniform waveguides (see Fig. 3.4). The developed samples are later post-baked at 120 °C for ~ 35 min.

Baking for longer time can induce cracks in the hardened PPR which can not effectively work as mask resulting in discontinuous waveguides.

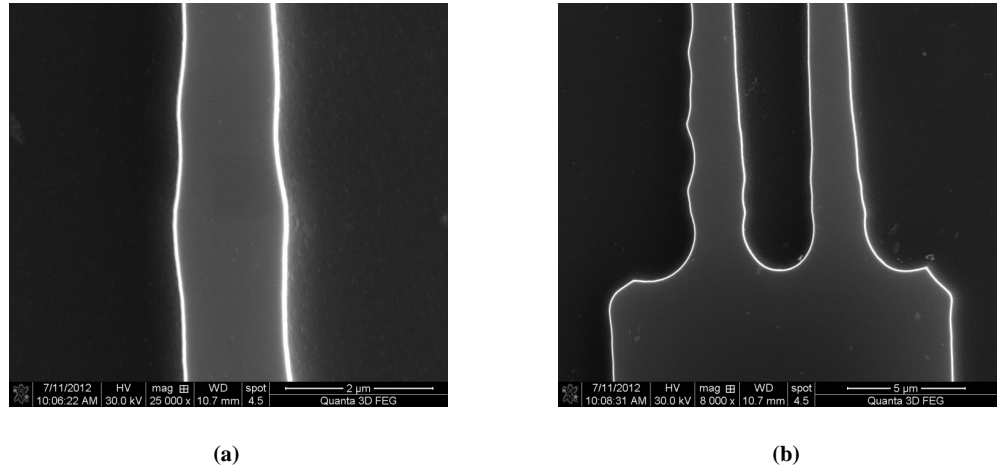


Figure 3.3: SEM images of a sample (IOL-UK 1) without post exposure bake: (a) straight waveguide (b) MMI coupler section in SOI.

(iv) Reactive Ion Etching

The rib structures are realized by etching un-masked silicon using OXFORD Plasma 80 Plus RIE system. As it can be seen in Fig. 3.2, the patterned PPR acts as mask for

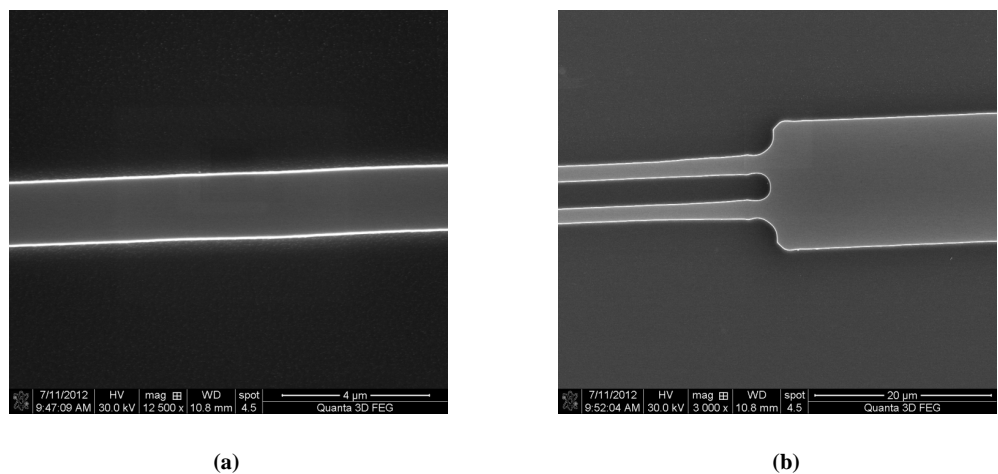


Figure 3.4: SEM images of sample (IOL-UK2) with post exposure bake: (a) straight waveguide (b) MMI coupler section.

realizing rib structure. Here, it is necessary to have anisotropic etching of silicon with better selectivity over the PPR mask. The etching chemistry optimized earlier is used for the present work [37, 47].

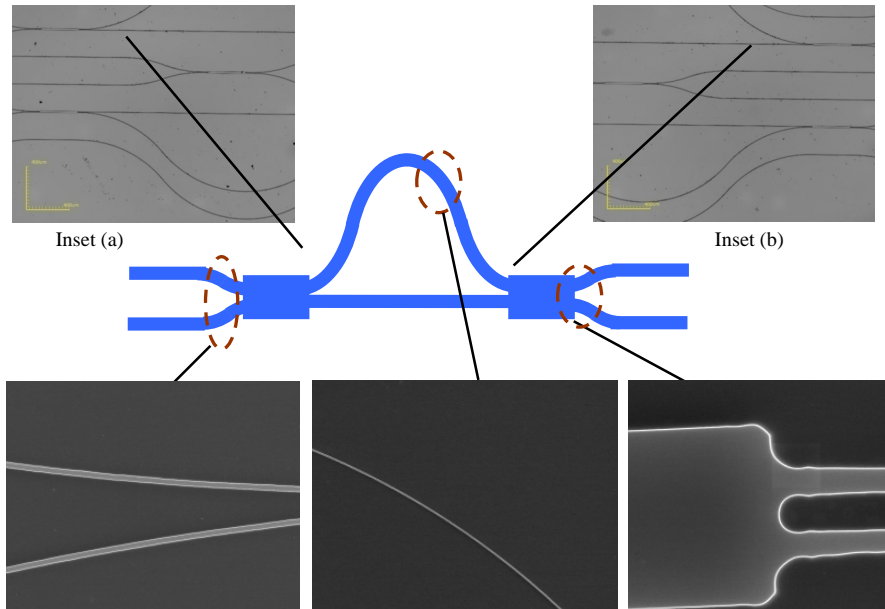


Figure 3.5: Typical SEM images of different sections of a fabricated interleaver. Inset (a) & Inset (b) : Confocal microscope images of MZI. The images correspond to sample IOL-UK 2

In this process, the sample is initially loaded into the chamber which is evacuated to obtain a base pressure of 3×10^{-7} mTorr. Then a mixture of SF_6 and Ar is passed, each at a flow rate of 20 sccm to achieve a constant chamber pressure of 200 mTorr. The oscillating electric field (RF freq: 13.56 MHz, RF power: 150 W) applied across the two electrodes inside the chamber, ionizes the gas (Ar) by stripping the electron and thereby creating plasma which eventually disintegrates SF_6 that etches silicon and releases SiF_4 . Our previous devices etched using the same recipe (SF_6 : Ar:: 20:20 sccm, 200 mTorr, RF Power: 150 W) showed a surface roughness of ~ 40 nm [37]. As mentioned earlier the RIE is carried out using patterned PPR acting as a mask over the sample surface, which is removed from top of rib structure after completion of etching process using acetone. Typical SEM images of different sections of MZI fabricated using PPR mask along with optimized process parameters discussed earlier are shown in Fig. 3.5.

As mentioned earlier, the RIE is carried out using patterned PPR acting as a mask over the sample surface, which is removed from top of the rib structure after completion

of etching process using acetone .

(vi) End-facet Preparation

The end facet of the fabricated samples have to be polished, to allow effective coupling of light into the waveguides and avoid scattering of light. The samples are mechanically polished using ULTRAPOL polishing Machine, Ultra-Tec Inc., USA. The end facet of the sample were initially polished using abrasive (diamond coated) films with particle size $30\ \mu\text{m}$. Subsequently, the abrasive films with smaller particle size ($15\ \mu\text{m}$, $9\ \mu\text{m}$,

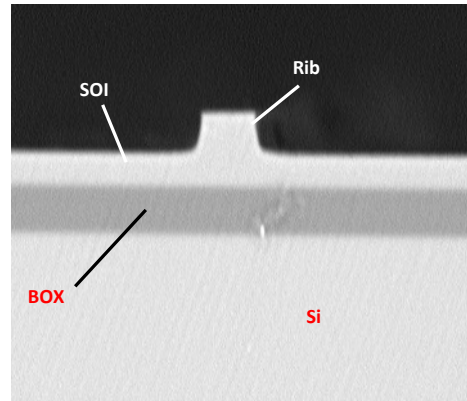


Figure 3.6: Polished end-facet of SOI based rib-waveguide cross -section $H = 2\ \mu\text{m}$, $\text{BOX} = 1\ \mu\text{m}$ and $W = \sim 2\ \mu\text{m}$

$6\ \mu\text{m}$, $3\ \mu\text{m}$, $1\ \mu\text{m}$, $0.5\ \mu\text{m}$, and $0.1\ \mu\text{m}$) were used and finally the end facet roughness of $\sim 0.1\ \mu\text{m}$ was achieved. The Fig. 3.6 shows the polished end-facets of a typical RCRW rib waveguide.

Note: IOL-UK 4 was fabricated using a different mask which had an equal MMI length of $353.5\ \mu\text{m}$.

Summary of Fabricated Devices

A list of fabricated samples is shown in Table 3.1. The width of the devices were varying depending on the etch-depth due to lateral etching ($\sim 15\%$). Some of the devices samples were damaged due to various issues in fabrication process like over-developing, discontinuous waveguides after RIE due to cuts in photo-resist pattern, edge

Table 3.1: List of fabricated samples. The etch-depth and working waveguides in each set ($S_i[n]$) are shown. Also see Fig. 3.1 for reference.

| Sample Number | Etch Depth [μm] | Device Sets: Uniform Waveguides | Remarks |
|---------------|------------------------------|---|---|
| IOL-UK1 | ~ 0.95 | | Devices were non-uniform showing wavy nature. None of the devices on the sample showed output response during optical characterization. |
| IOL-UK2 | ~ 0.98 | S1:Wg3-Wg10; S2:Wg1-Wg4; S2:Wg7-Wg10; S3:Wg1,Wg2 | Set 1 MMI coupler showed about 35:65 splitting whose MZI showed an extinction of about 6 dB for TM pol., Set 2 MMI was damaged during fabrication however MZI showed an extinction of 10 dB for TM pol. |
| IOL-UK3 | ~ 1.07 | | Devices were discontinuous as the mask was damaged hence a new mask was fabricated |
| IOL-UK4 | ~ 1.1 | S1:Wg5-Wg10; S2:Wg1-Wg10; S3:Wg1-Wg6 | Reference MMI coupler showed nearly 3-dB power splitting. MZI was showing an extinction of 10 dB for both pol. |

damage and sample breaking during dicing/polishing, high surface roughness after RIE due to previous process residue, etc.

3.3 Waveguide Properties: Experimental Results

The waveguide loss measurement was carried out using low-finesse loss measurement technique, in the optical characterization setup available at our lab. A schematic of the end-fire coupling setup is shown in Fig. 3.7.

An external cavity tunable semiconductor laser source ($1520 \text{ nm} < \lambda < 1600 \text{ nm}$) with a line width of $\sim 0.8 \text{ pm}$ and minimum tuning step of 1 pm is used to characterize the fabricated devices. The light output from the source is passed through a polarization controller using a single mode fiber. The polarization controller induces stress on the single mode fiber due to which the power can be varied among the two orthogonal

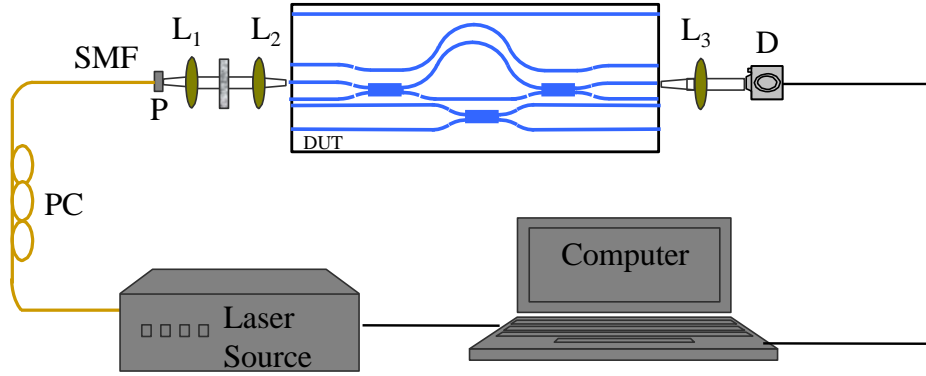


Figure 3.7: Schematic of the experimental setup used for characterization of integrated optical interleaver. PC-Polarization Controller, SMF-single mode fiber, L-Lens, P-Polarizer, DUT-Device Under Test, D-Detector (IR Camera/PIN detector).

polarizations. The light beam is then collimated using a lens setup and allowed to pass through a Glan-Thompson polarizer. The polarized light beam is then focused on the polished end facet of the rib waveguide. The transmitted light from the device is collected using another lens and focused on the detector/IR camera for measuring the power/intensity profiles. The data-logging from detector/IR camera and wavelength tuning at the laser source are synchronized using a LABVIEW program.

The single-mode straight waveguides fabricated along side interleaver were studied for waveguide loss and polarization dependency. These waveguides were ~ 1.5 cm long with $W = 1.6 \mu\text{m}$ and $h = 1.1 \mu\text{m}$. The captured intensity profiles for TE and TM polarization are shown in Fig. 3.9. The measured $(1/e^2)$ mode size for TE (TM) polarization is found to be $\sim 3.3 \mu\text{m} \times 2.2 \mu\text{m}$ ($\sim 2.7 \mu\text{m} \times 2.3 \mu\text{m}$). Our theoretical simulations show a mode-size of $\sim 1.55 \mu\text{m} \times 1.62 \mu\text{m}$ ($\sim 1.52 \mu\text{m} \times 1.55 \mu\text{m}$) for TE(TM) polarizations, respectively. A deviation in experimental results compared to theoretical simulations is expected to be due to non-vertical side wall and errors during mode-profile measurements (see Fig. 3.6).

The waveguide width and etch-depth of the waveguides of the two working samples were obtained using confocal microscope and tabulated in the Table 3.2 below:

Waveguide loss was measured using Fabry-perot method that can then be derived using Eq. 3.1 [48, 49].

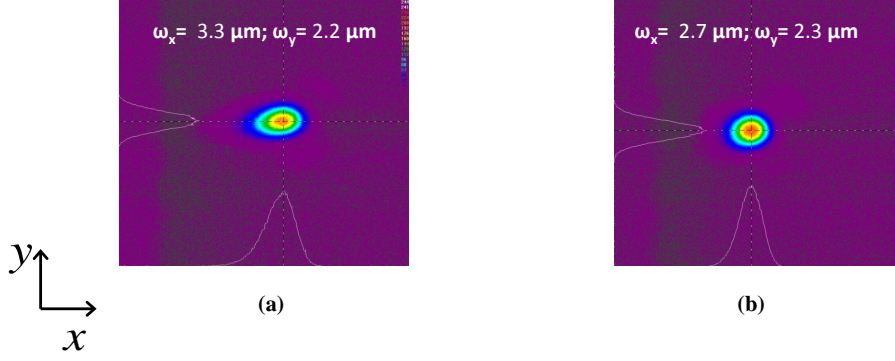


Figure 3.8: Captured intensity profiles for TE (a), and TM (b) polarizations, respectively. ω_x is the mode spread in horizontal direction and ω_y is the mode spread in vertical direction. Results correspond to set S3 of sample IOL-UK4.

Table 3.2: Waveguide dimensions and calculated birefringence in different samples

| Device | Waveguide width [μm] | Etch-depth [μm] | Estimated Birefringence |
|---------|-----------------------------------|------------------------------|-------------------------|
| IOL-UK2 | ~ 1.73 | 0.98 | 1.748×10^{-3} |
| IOL-UK4 | ~ 1.64 | 1.1 | 8.66×10^{-4} |

$$\alpha = \frac{1}{L} \ln \left(\frac{1}{R} \frac{\sqrt{\zeta} - 1}{\sqrt{\zeta} + 1} \right) \quad (3.1)$$

where, α is the loss, $\zeta = \frac{I_{max}}{I_{min}}$, L is the sample length and R is reflectivity at the end-facet. The values of I_{max} and I_{min} , the maximum and minimum values of the intensities respectively and reflectivity is given by $R = \left(\frac{n_{eff}-1}{n_{eff}+1} \right)^2$. Where n_{eff} is the effective index of the waveguide at $\lambda \sim 1550 \text{ nm}$.

The best of the measured waveguide loss for TE (TM) polarization using the above equation is 0.46 dB/mm (0.42 dB/mm). This waveguide loss accounts for material absorption characteristics and scattering loss due waveguide side-wall roughness. The waveguide losses are higher in case of TE polarized light as the dominant electric field component normal to the rib side wall experiences higher scattering.

The 1.4 cm-long meander bends replicating the top arm of the MZI were also characterized for its insertion loss. These meander bend structures showed an overall wave-

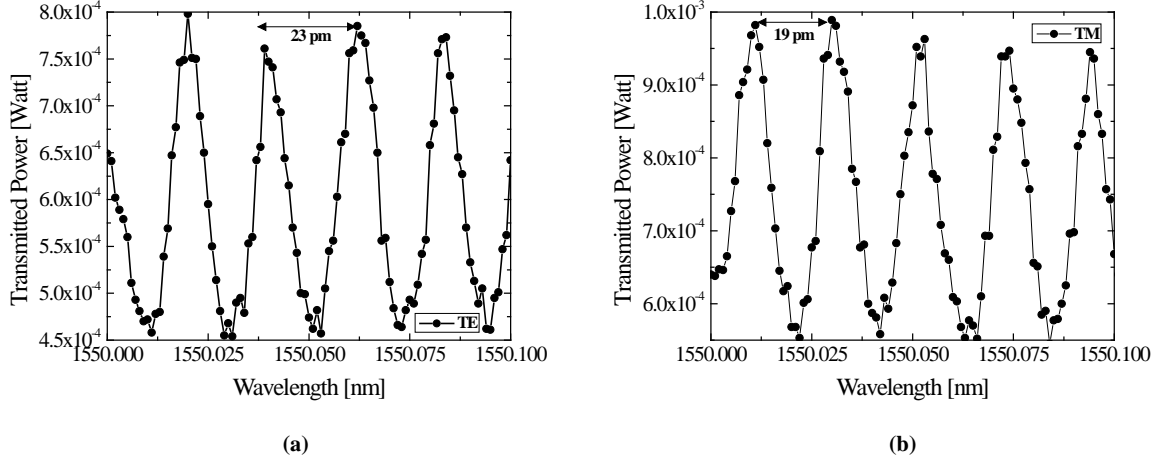


Figure 3.9: Fabry-Perot response recorded for a RCRW for TE (a), and TM (b) polarizations, respectively.

length independent insertion loss of ~ 15.6 dB (~ 13.7 dB) for TE(TM) polarizations. These structures contain four s-bend structures of 1 mm bending radius. Deducting the measured waveguide loss for such a ~ 1.4 cm long straight waveguide, a total bend induced loss of ~ 9 dB (~ 7.8 dB) (with 4 s-bends) is estimated for TE(TM) polarizations.

3.4 Conclusions

Mask design and Fabrication was carried out to realize $2\text{-}\mu\text{m}$ waveguide structures on SOI platform. End-facets were prepared for optical characterization of the devices. Waveguide loss and mode-size were measured using our end-fire coupling technique. The loss of the waveguide was observed to be ~ 4 dB/cm for both polarizations. The higher loss is expected due to side-wall roughness, which can be reduced by using ICP-RIE.

CHAPTER 4

Device Characterizations

The fabricated MMI couplers and asymmetric MZIs (interleavers) were characterized in terms of insertion loss, wavelength & polarization dependencies, and inter-channel extinctions. The experimental setup shown in Fig. 3.7, has been modified accordingly. At first, characterization results of MMI couplers will be presented. Later, the interleaver characteristics of asymmetric MZIs have been presented and discussed.

4.1 MMI Coupler

The 2×2 reference MMI couplers adjacent to the MZI were characterized for insertion loss, polarization and wavelength dependent throughput. Transmitted powers and intensity profiles measured at two output ports indicates uniform power splitting of MMI couplers (see Fig. 4.1). The splitting of the MMI coupler was then recorded over the entire $\lambda = 1520$ nm to 1600 nm band. As expected from our theoretical predictions, MMI couplers showed a polarization independent and uniform power splitting across the entire C+L band (see Fig. 4.2) [29].

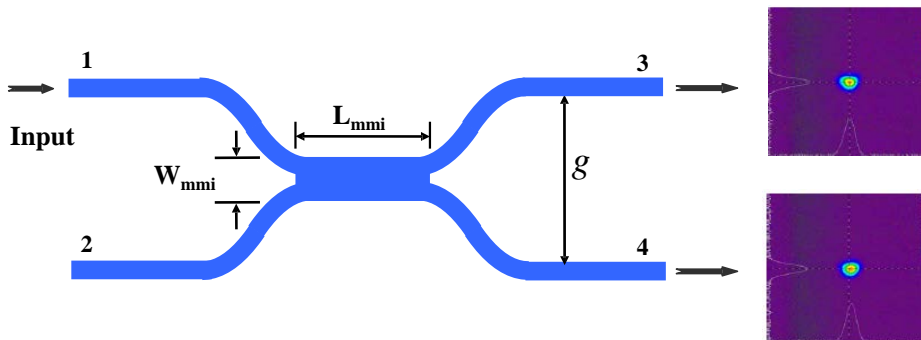


Figure 4.1: Captured intensity profiles at the two output ports of a MMI coupler showing uniform power splitting at bar (Port 3) and cross (Port 4) port. The profiles are recorded at $\lambda = 1550$ nm for TE polarization from MMI coupler in set S2 of IOL-UK4.

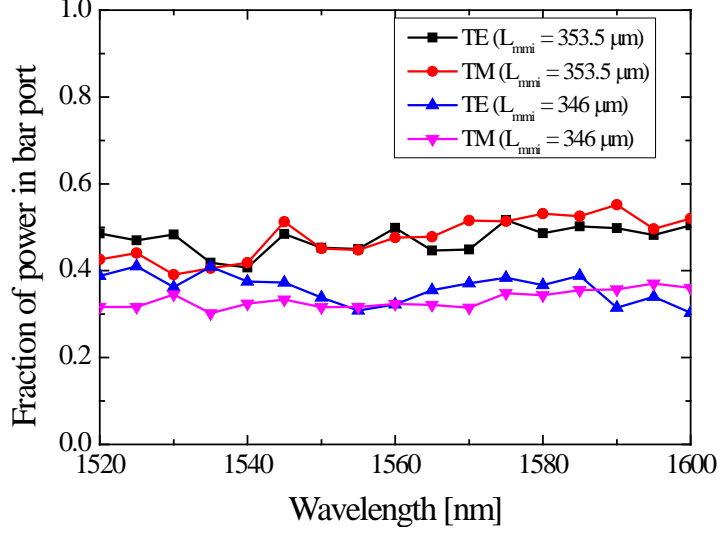


Figure 4.2: Wavelength dependent throughput fraction of power in bar port of MMI couplers with (a) $L_{mmi} = 346 \mu\text{m}$, and (b) $L_{mmi} = 353.5 \mu\text{m}$. Note the difference in splitting ratio for MMI lengths. These results are recorded from MMI couplers in set S1 of IOL-UK2 and set S2 of IOL-UK4, respectively.

In our actual design, MMI length was fixed as $L_{mmi} = 346 \mu\text{m}$. Experimental results showed an power splitting ratio of 35:65 at bar and cross ports respectively for the designed MMI. We have used a correction factor for length of MMI (δL_{mmi}), using an analytic expression [45]. This correction factor is chosen to overcome the fabrication error and obtain the expected response. The correction factor was chosen as $\delta L_{mmi} = 7.5 \mu\text{m}$, based on our calculations. Hence, apart from the actual design value of L_{mmi} , we have placed two other MZI structures with MMI lengths of $L_{mmi} + \delta L_{mmi}$ and $L_{mmi} + 2\delta L_{mmi}$, respectively on our mask. Our experimental results show that MMI coupler having an corrected length of $L_{mmi} + \delta L_{mmi}$, shows a nearly polarization and wavelength independent 3-dB power splitting (see Fig. 4.2).

The overall insertion loss of the MMI based coupler $L_{mmi} = 353.5 \mu\text{m}$ was estimated to be ~ 13.2 dB (nearly polarization independent). This includes waveguide losses, total bending losses and, insertion loss of coupler.

4.2 Mach-Zehnder Interferometer

The transmitted mode profiles at the two output ports were captured using IR-camera in the near field. Fig. 4.3 shows the transmitted profiles for TE polarizations at two consecutive wavelengths with 100 GHz channel spacing [50].

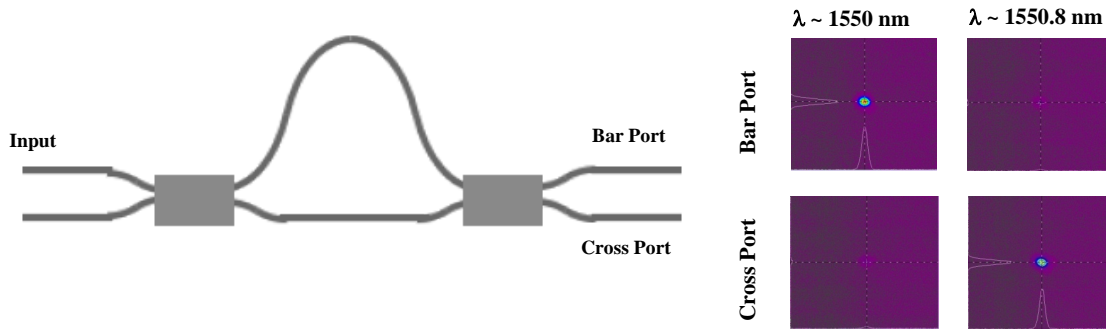


Figure 4.3: Transmitted intensity profiles measured at bar and cross ports for two different wavelengths: (a) $\lambda = 1550$ nm and (b) $\lambda = 1550.8$ nm for TE polarization, respectively.

It is clearly evident that when one of the channel retains power in a particular port, the same channel in other port is completely diminished. The interleavers were characterized for wavelength dependency across the entire optical C+L band. Fig. 4.4 shows the device response over entire optical C band recorded using LAB VIEW with a tuning

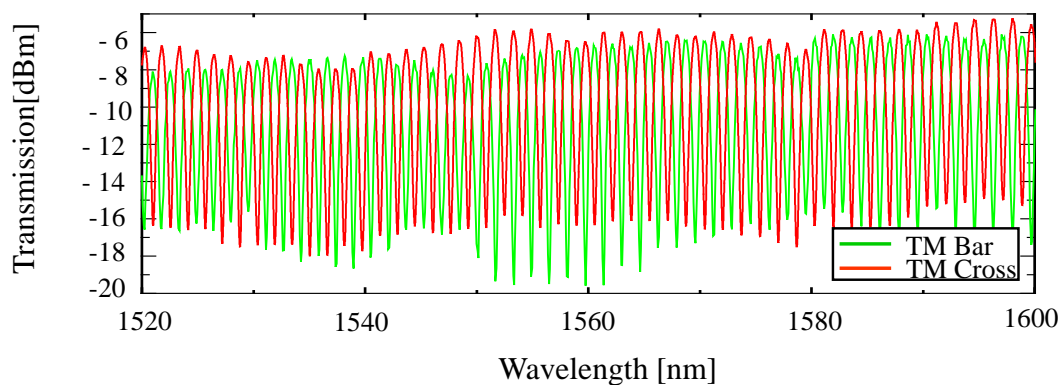


Figure 4.4: Transmission characteristics of an asymmetric MZI interleaver over entire optical C band (set S2 of the sample IOL-UK2). The experimentally measured value of channel spacing $\Delta\lambda = 0.8$ nm and inter-channel extinction $\delta_{ex_ch} \sim 10$ dB. The green color correspond to response at Port 3 (Bar) and, the red color correspond to response at Port 4 (cross). Laser wavelength tuning steps = 80 pm.

step of 80 pm.

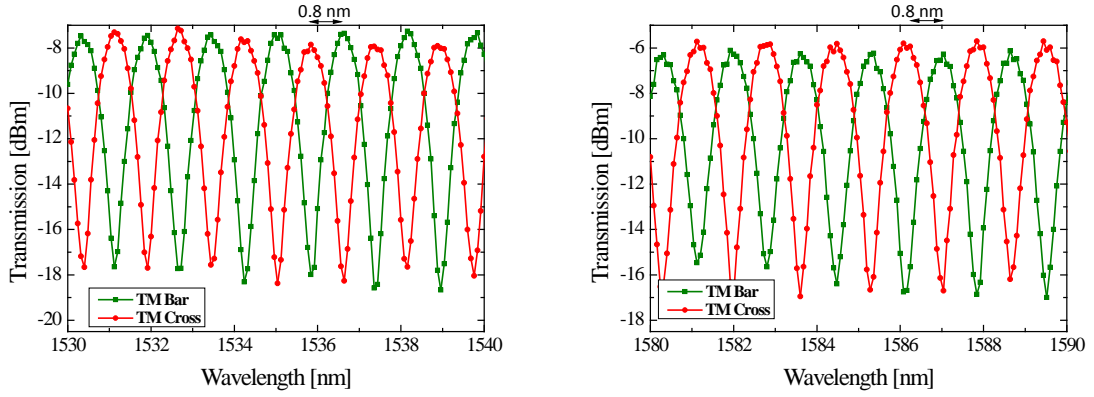


Figure 4.5: Measured transmission characteristics for TM polarization. Lines in green correspond to response at Port 3 (Bar) and, lines in red correspond to response at Port 4 (cross). Results correspond to interleaver in set S2 of IOL-UK2.

Uniformity of the response in terms of inter-channel extinction and insertion loss at the channel peak is clearly evident from Fig 4.4. It is worth to mention here that the two MMI couplers in this particular structure response shown here were having a length of $353.5 \mu\text{m}$. Two small bands (1530 nm - 1540 nm and 1580 nm - 1590 nm) of the complete characteristics is represented in Fig. 4.5 to show that the response is nearly uniform with the value of channel spacing $\Delta\lambda = 0.8 \text{ nm}$ and inter-channel extinction $\delta_{ex_ch} \sim 10 \text{ dB}$ at both the output ports of the MZI.

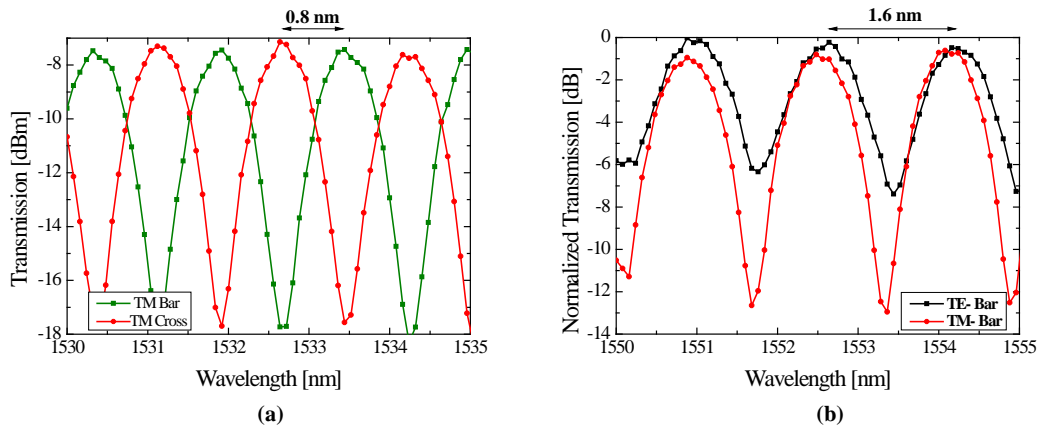


Figure 4.6: Measured transmission characteristics for TM polarization (a) and, polarization dependent characteristics (b), respectively. The reference MMI couplers show nearly uniform power splitting ($L_{mmi} = 353.5 \mu\text{m}$ and etch depth $\sim 1 \mu\text{m}$). Note that the resonance peaks for both polarizations are overlapping, the results correspond to set 4 of sample IOL-UK2.

Four different samples have been fabricated, among which two samples (IOL-UK2 and IOL-UK4) have working MZIs. The MZI having a MMI length of $353.5 \mu\text{m}$ showed an inter-channel extinction $\delta_{ex_ch} \sim 10 \text{ dB}$ at both the output ports of the MZI for TM polarization (see Fig. 4.6(a) and Fig. 4.7(b)). For TE polarization, devices in sample IOL-UK2 and sample IOL-UK4 showed an inter-channel extinction $\delta_{ex_ch} \sim 6 \text{ dB}$ (see Fig. 4.6(b)) and $\delta_{ex_ch} \sim 10 \text{ dB}$ (see Fig. 4.7(b)), respectively. The polarization dependent characteristics of the MZI show the resonance peak shift due to the birefringence of the waveguide as expected from our simulations. Birefringence in sample IOL-UK2 (refer Table. 3.2) leads to a resonance peak shift of 0.8 nm for TE polarization w.r.t TM polarization in MZI response. This leads to the overlap of TE and TM response (see Fig. 4.6(b)). In case of sample IOL-UK4 the birefringence (given in Table. 3.2) leads to a resonance peak shift of $\sim 0.4 \text{ nm}$ for TE polarization w.r.t TM polarization which is clearly evident from the response in Fig. 4.7(b)

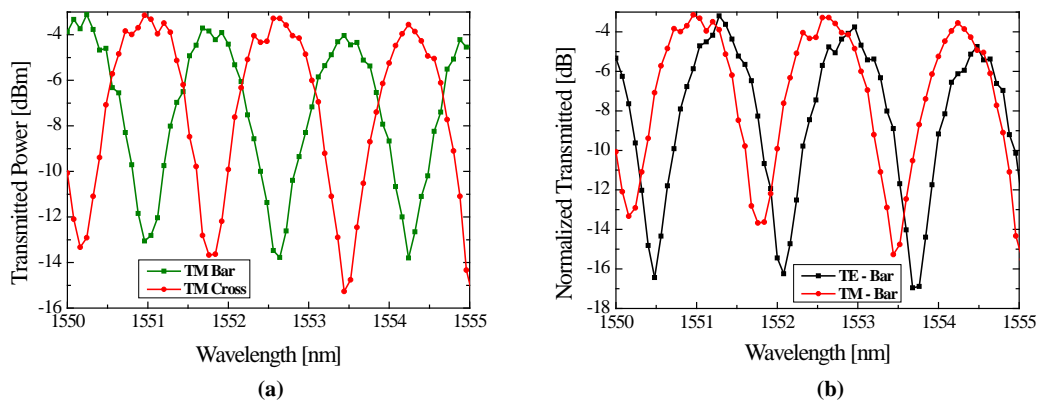


Figure 4.7: (a) Experimentally measured transmission characteristics for TM polarization, (b) polarization dependent characteristics of asymmetric MZI in IOL-UK4. The reference MMI couplers show nearly uniform power splitting ($L_{mmi} = 353.5 \mu\text{m}$ and $etchdepth \sim 1 \mu\text{m}$). Note the shift in resonance peaks for both polarizations, the results correspond to set 2 of sample IOL-UK4.

The low inter-channel extinction in MZI (see Fig. 4.4(a)) is due to resolution error caused by high wavelength tuning step ($\sim 80 \text{ pm}$). For better wavelength characteristics we have recorded the response of the MZI using optical spectrum analyzer, with the setup shown in Fig. 4.8. The MZI response in OSA (see Fig. 4.9(b)) showed an inter channel extinction of $\sim 15 \text{ dB}$ (at a tuning resolution of 0.8 pm) when excited by a broadband source. An external broadband LED source ($1310 \text{ nm} < \lambda < 1620 \text{ nm}$) with a output power of 2 mW (for $\lambda \sim 1550 \text{ nm}$) is connected to the EDFA (wave-

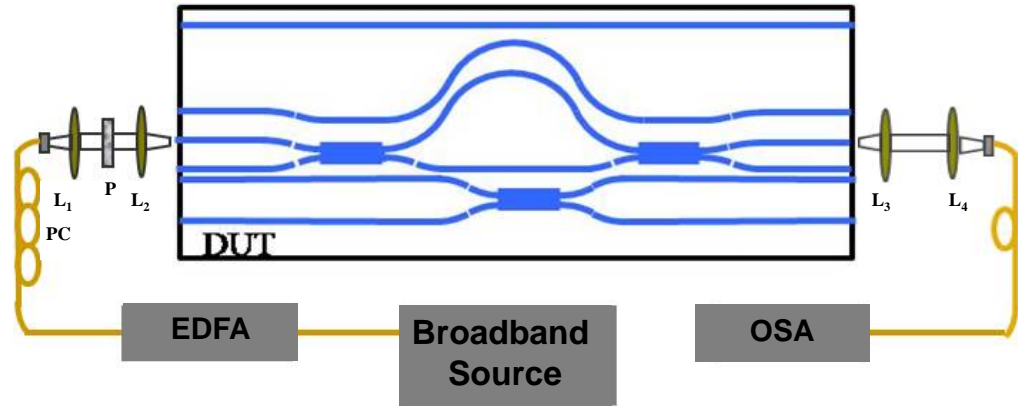
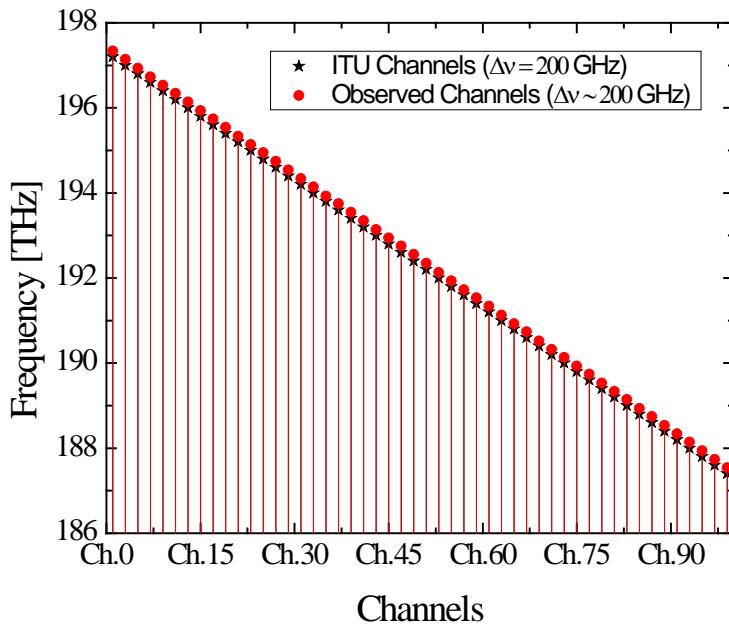


Figure 4.8: Schematic of the experimental setup used for characterization of integrated optical interleaver. PC-Polarization Controller, SMF-single mode fiber, L-Lens, P-Polarizer, DUT-Device Under Test, EDFA-Erbium Doped Fiber Amplifier, OSA- Optical Spectrum Analyzer).

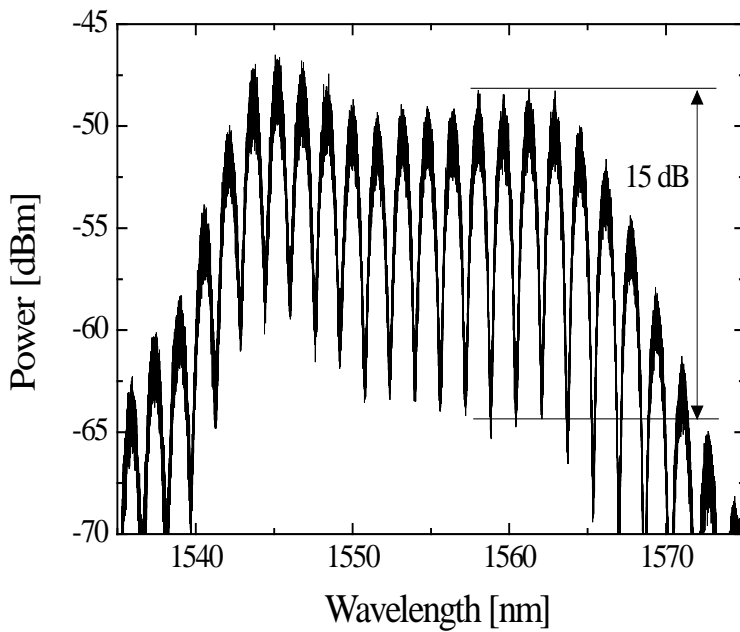
length range: 1535-1565nm, pump wavelength: 971nm, max output power : 2 Watt). The light output from the EDFA is taken through a polarization controller using a single mode fiber. The light beam is then collimated using a lens setup and allowed to pass through a Glan-Thompson polarizer. The polarized light beam is then focused on the polished end facet of the rib waveguide. The transmitted light from the device is collected using another lens and coupled to the single-mode fiber, which is then fed into the OSA (wavelength measurement range: 1520 nm - 1630 nm, tuning step: ~ 0.8 pm), minimum detectable power: -70 dBm) for recording the device response.

Calculations from transmitted characteristics shows that the fabricated MZI indeed separates incoming ITU channels with 100 GHz spacing at the two output ports (see in Fig. 4.9 (a)). The MZIs were also characterized for insertion loss. The overall insertion loss of ~ 15 dB was measured at the channel pass band. This high insertion loss accounts for waveguide losses (~ 4 dB/cm), bend induced losses (~ 8 dB) and insertion loss of two MMI couplers (~ 3 dB).

The MZI were also characterized for insertion loss. The overall insertion loss of ~ 15 dB was measured at the channel pass band. This high insertion loss accounts for waveguide losses (~ 4 dB/cm), bend induced losses (~ 8 dB) and insertion loss of two MMI couplers (~ 3 dB).



(a)



(b)

Figure 4.9: (a) ITU channels and experimental resonant frequencies observed at cross port of MZI (set 4 of sample IOL-UK2) for TM polarization, (b) measured wavelength dependent characteristics of MZI (set 2 of sample IOL-UK4) using high-resolution OSA for broadband input ($\lambda = 1535$ to 1565 nm) showing an inter-channel extinction of ~ 15 dB for TM polarization

4.3 Conclusions

A compact multi-mode interference coupler based 2×2 Mach-Zehnder interferometer for interleaver applications has been successfully fabricated in SOI platform with reduced cross-section single-mode rib waveguide structures. The characterization results show an inter-channel extinction of ~ 15 dB at bar and cross ports with an interleaved channel spacing of ~ 200 GHz.

CHAPTER 5

Conclusions

5.1 Summary

This thesis deals with a design, fabrication and characterization of MMI based devices like power splitter and DWDM channel interleaver. In this chapter, the summary of research outcome has been discussed and it has been followed by an outlook. Various design parameters for single-mode straight waveguides, bend waveguides and, MMI couplers have been optimized for compact, dispersion-free Mach-Zehnder Interferometer for wavelength filtering applications. Afterwards, an integrated optical MMI based compact MZI on reduced cross-section SOI rib waveguides has been successfully demonstrated.

The characterized device samples showed an inter-channel extinction of ≥ 10 dB at both ports with an interleaved channel spacing of ~ 200 GHz. The devices are found to be fabrication sensitive which changes the birefringence of the waveguide and lead to shift in resonance peaks of TE and TM polarizations. The characterized waveguides showed a relatively high loss of ~ 4.6 dB/cm (~ 4.2 dB/cm) for TE(TM) polarization, this is because of the higher surface roughness due to reactive ion etching. Use of ICP-RIE, for etching may reduce the surface roughness and hence can lead to lower waveguide loss and device insertion loss. The Insertion loss of the meander bend structure (includes 4 S-bends with bending radius of 1 mm) is found to be ~ 9.1 dB/cm (~ 7.8 dB/cm) for TE(TM) polarization. MMI coupler showed an insertion loss of ~ 13.2 dB for both the polarizations which includes bend and waveguide loss.

The length of the 2×2 MMI based 3-dB power splitter was about ~ 353.5 μm , while the length of overall MMI based MZI is about 5.2 mm. The fabricated MZI showed an overall insertion loss of ~ 15 dB at the channel resonance peak. This includes, waveguide loss (~ 4.2 dB), bend-induced losses (~ 2.25 dB/bend) and insertion loss of ~ 3 dB for each MMI couplers.

The fabricated MZI were found to be slightly polarization sensitive due to the asymmetric cross-sectional geometry of reduced cross-section rib waveguides. As a result, the resonance peaks in transmission characteristics of interleaver when operated for two different polarization (TE and TM) were found to be shifted. One of the fabricated MZI response has been recorded using an OSA. The response showed an inter-channel extinction of > 15 dB (at a resolution of 0.8 pm) at either of the ports with an insertion loss of ~ 15 dB at channel resonance peaks.

5.2 Outlook

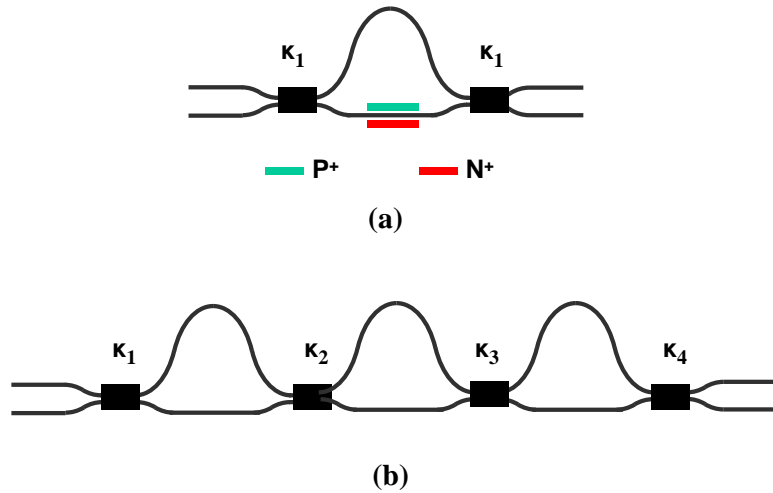


Figure 5.1: (a) MZI integrated with PIN structure, and (b) Higher order 3- stage lattice type filter using MZI to achieve band flattening. κ_i is the coupling ratio of the MMI coupler, which is a crucial parameter in the higher order filter design.

Integrating a ring structure with an RCRW based MZI, may be carried out to achieve flat-band response. Alternatively, such interleavers can be designed with RCRW-based asymmetric MZI. RCRW based devices can provide improved polarization and inter channel extinctions compared to LCRW, with smaller foot-prints due to tighter confinement of the guided mode. Moreover, re-configurable interleavers can be demonstrated by having an external heating element integrated with the package or an on-chip NiCr heater. Reconfigurability can also be achieved by integrated electro-optic element (PIN-structure). PIN structure can be integrated in one of the arm of the MZI (see Fig. 5.1(a)),

refractive index in one arm can be tuned by applying voltage to the PIN structure.

The response of a single MZI is sinusoidal, which results in a narrow pass band. Hence, most of the available spectrum remains unused. Ideally, rectangular response is desired but cannot be achieved because of causality. One approach for achieving flat-top response is by integrating a ring-resonator with the MZI structure [51]. Another approach to achieve a nearly ideal response is by using resonant couplers or multi-stage lattice filters (as shown in Fig. 5.1(b)). The basic lattice element of such a higher order filter is an asymmetric 2×2 MZI. One may further investigate on the MMI coupler by changing the design parameters and achieve compact structure.



APPENDIX A

Appendix

A.1 Asymmetric MZI Based Interleaver

Transfer Function of Asymmetric MZI

Considering Fig. 2.1, the electric field at different points in upper (lower) arm of MZI are marked as E_{1i} (E_{1j}). Consider M_{3-dB} , M_ϕ and M_{3-dB} are the transfer matrix of first 3-dB coupler, the unbalanced arms and second 3-dB coupler, respectively (see Fig. 2.1). Then the transfer matrix solution for the MZI can be derived as below.

$$M_{3-dB} = \begin{bmatrix} E_{12} \\ E_{22} \end{bmatrix} = \begin{bmatrix} \frac{1}{\sqrt{2}} & -j\frac{1}{\sqrt{2}} \\ -j\frac{1}{\sqrt{2}} & \frac{1}{\sqrt{2}} \end{bmatrix} \cdot \begin{bmatrix} E_{11} \\ E_{21} \end{bmatrix} \quad (\text{A.1})$$

$$M_\phi = \begin{bmatrix} E_{13} \\ E_{23} \end{bmatrix} = e^{-j\beta L} \begin{bmatrix} \exp(-j\phi) & 0 \\ 0 & \exp(j\phi) \end{bmatrix} \cdot \begin{bmatrix} E_{12} \\ E_{22} \end{bmatrix} \quad (\text{A.2})$$

$$M_{3-dB} = \begin{bmatrix} E_{14} \\ E_{24} \end{bmatrix} = \begin{bmatrix} \frac{1}{\sqrt{2}} & -j\frac{1}{\sqrt{2}} \\ -j\frac{1}{\sqrt{2}} & \frac{1}{\sqrt{2}} \end{bmatrix} \cdot \begin{bmatrix} E_{13} \\ E_{23} \end{bmatrix} \quad (\text{A.3})$$

Let M be the transfer matrix of asymmetric MZI based interleaver then, $M = M_{3-dB} \cdot M_\phi \cdot M_{3-dB}$. Now, considering $\hat{M} = M_\phi \cdot M_{3-dB}$ then

$$\begin{bmatrix} E_{13} \\ E_{23} \end{bmatrix} = e^{-j\beta L} \begin{bmatrix} \frac{1}{\sqrt{2}} & -j\frac{1}{\sqrt{2}} \\ -j\frac{1}{\sqrt{2}} & \frac{1}{\sqrt{2}} \end{bmatrix} \cdot \begin{bmatrix} \exp(-j\phi) & 0 \\ 0 & \exp(j\phi) \end{bmatrix} \cdot \begin{bmatrix} E_{11} \\ E_{21} \end{bmatrix} \quad (\text{A.4})$$

$$\hat{M} = \frac{e^{-j\beta L}}{\sqrt{2}} \begin{bmatrix} \exp -j\Phi & -j \exp j\Phi \\ -j \exp -j\Phi & \exp j\Phi \end{bmatrix} \cdot \begin{bmatrix} \exp(-j\phi) & 0 \\ 0 & \exp(j\phi) \end{bmatrix} \quad (\text{A.5})$$

$$\hat{M} = e^{-j\beta L} \begin{bmatrix} 2j \sin \phi & 2j \cos \phi \\ 2j \cos \phi & -2j \sin \phi \end{bmatrix} \quad (\text{A.6})$$

Now, for $M = M_{3-dB} \cdot \hat{M}$ then

$$\hat{M} = \frac{e^{-j\beta L}}{\sqrt{2}} \begin{bmatrix} 0.707 & -0.707j \\ 0.707j & 0.707 \end{bmatrix} \cdot \begin{bmatrix} \exp -j\Phi & -j \exp j\Phi \\ -j \exp -j\Phi & \exp j\Phi \end{bmatrix} \quad (\text{A.7})$$

$$E_{14} = \exp(-j\beta L)(E_{11} \cdot \sin \phi + E_{21} \cdot \cos \phi)j \quad (\text{A.8})$$

$$E_{24} = \exp(-j\beta L)(E_{11} \cdot \cos \phi + jE_{21} \cdot \sin \phi)j \quad (\text{A.9})$$

The power can then be given as,

$$P_{14} = (E_{11}^2 \cdot \sin^2 \phi + E_{21} \cdot E_{11} \cdot \sin(2\phi) + (E_{21}^2 \cdot \cos^2 \phi) \quad (\text{A.10})$$

$$P_{14} = (E_{11}^2 \cdot \cos^2 \phi + E_{21} \cdot E_{11} \cdot \sin(2\phi) + (E_{21}^2 \cdot \sin^2 \phi) \quad (\text{A.11})$$

Here, the 2ϕ terms in Eq. A.10 and A.11 correspond to the harmonics with wavelength $\frac{\lambda}{2}$. In our case, we are considering the wavelengths in optical band $\lambda = 1520 - 1600$ nm. The $\frac{\lambda}{2}$ wavelengths produced as a result of beating of two signals with different phase are absorbed due to optical properties of silicon.

Interleaver Channel Spacing

The schematic of Mach-Zehnder Interferometer for interleaver application is shown in Fig. 2.1. Assume that the two consecutive WDM channels (λ_1 and λ_2) are given at its input. The effective refractive index of two channel wavelengths is n_1 and n_2 . The phase accumulated by channel λ_1 while propagating in two arms can be given as below.

$$\lambda_1 \phi_1 = \frac{2\pi n_1 L_1}{\lambda_1} \quad (\text{A.12})$$

$$\lambda_1 \phi_2 = \frac{2\pi n_1 L_2}{\lambda_1} + \left(\frac{\pi}{2}\right)_{MMI1} + \left(\frac{\pi}{2}\right)_{MMI2} \quad (\text{A.13})$$

Similarly, for channel λ_2

$$\lambda_2 \phi_1 = \frac{2\pi n_2 L_1}{\lambda_2} \quad (\text{A.14})$$

$$\lambda_2 \phi_2 = \frac{2\pi n_2 L_2}{\lambda_2} + \left(\frac{\pi}{2}\right)_{MMI1} + \left(\frac{\pi}{2}\right)_{MMI2} \quad (\text{A.15})$$

It is required that λ_1 exists in Port 3 only and hence from A.12, A.13,

$$\lambda_1 \phi = \lambda_1 \phi_1 - \lambda_1 \phi_2 = 2l\pi \quad (\text{A.16})$$

$$\Rightarrow \frac{2\pi n_1 L_1}{\lambda_1} - \frac{2\pi n_1 L_2}{\lambda_1} + \pi = 2l\pi \quad (\text{A.17})$$

$$\Rightarrow \frac{2\pi n_1 \Delta L}{\lambda_1} + \pi = 2l\pi \quad (\text{A.18})$$

Similarly,

$$\lambda_2 \phi = \lambda_2 \phi_1 - \lambda_2 \phi_2 = (2m - 1)\pi \quad (\text{A.19})$$

$$\Rightarrow \frac{2\pi n_2 L_1}{\lambda_2} - \frac{2\pi n_2 L_2}{\lambda_2} + \pi = 2l\pi \quad (\text{A.20})$$

$$\Rightarrow \frac{2\pi n_2 \Delta L}{\lambda_2} + \pi = (2l - 1)\pi \quad (\text{A.21})$$

here, l and m are integers. If λ_1 exists in only Port 3 and λ_2 only in Port 4, then,

$$\lambda_1 \phi - \lambda_2 \phi = \pi \quad (\text{A.22})$$

$$\Rightarrow \frac{2\pi n_1 \Delta L}{\lambda_1} + \pi - \frac{2\pi n_2 \Delta L}{\lambda_2} + \pi = \pi \quad (\text{A.23})$$

$$\Rightarrow 2\pi \Delta L \left(\frac{n_2}{\lambda_2} - \frac{n_1}{\lambda_1} \right) = \pi \quad (\text{A.24})$$

$$\Rightarrow \Delta L = \frac{\lambda_1 \cdot \lambda_2}{2\Delta \lambda n_g} \quad (\text{A.25})$$

In order to design an MZI for interleaver applications we need to maintain the channel spacing ($\Delta\nu$) constant. Hence we replace $\Delta\lambda$ by $\Delta\nu$, the above equation (Eq. A.25) can be written as

$$\Delta L = \frac{c}{2\Delta\nu n_g} \quad (\text{A.26})$$

Where c is the velocity of light in free space and n_g is the group-index of the waveguide. This equation Eq. A.26 was used to choose the value of ΔL for the design of MZI.

A.2 Recipes for etching

Recipes used for etching of various materials during the fabrication process are mentioned below.

Dry etching of Silicon

The dry etching of Si has been done using conventional RIE technique.

Recipe: Ar/SF₆:: 20/20 sccm

Chamber Pressure: 200 mTorr

RF Power: 150 W

PPR Ashing

PPR ashing is often carried using conventional RIE technique. This is done to remove residual PPR on top of wafer, which could not be removed by acetone.

Recipe: O₂:: 35 sccm

Chamber Pressure: 250 mTorr

RF Power: 150 W

REFERENCES

- [1] M. T. Bohr, "Interconnect scaling-the real limiter to high performance ulsi," in *IEEE International Electron Devices Meeting (IEDM)*, pp.241–244, 1995.
- [2] R. Ho, K. W. Mai, and M. A. Horowitz, "The future of wires," *Proc. IEEE*, vol. 89, no. 4, pp. 490–504, 2001.
- [3] S. I. Association, *National technology roadmap for semiconductors*, 1997.
- [4] J. Cong, "Challenges and opportunities for design innovations in nanometer technologies," *SRC Design Sciences Concept Paper*, vol. 12, 1997.
- [5] M. Haurylau, G. Chen, H. Chen, J. Zhang, N. A. Nelson, D. H. Albonese, E. G. Friedman, and P. M. Fauchet, "On-chip optical interconnect roadmap: Challenges and critical directions," *IEEE J. of Quan. Electron.*, vol. 12, no. 6, pp. 1699 –1705, Dec. 2006.
- [6] A. C. Cangellaris, "The interconnect bottleneck in multi-ghz processors; new opportunities for hybrid electrical/optical solutions," in *IEEE Proc. Fifth International Conference on Massively Parallel Processing*, pp. 96–103, 1998.
- [7] R. Kirchain and L. Kimerling, "A roadmap for nanophotonics," *Nat. Photon.*, vol. 1, no. 6, pp. 303–305, 2007.
- [8] B. Dhoedt, R. Baets, P. Van Daele, P. Heremans, J. Van Campenhout, J. Hall, R. Michalzik, A. Schmid, H. Thienpont, and R. Vounckx, "Optically interconnected integrated circuits to solve the cmos interconnect bottleneck," in *48th IEEE Electronic Components & Technology Conference*, pp. 992 – 998, 1998.
- [9] S. Assefa, W. Green, A. Rylyakov, C. Schow, F. Horst, and Y. Vlasov, "Cmos integrated silicon nanophotonics: enabling technology for exascale computational systems," in *Proceedings of the Optical Fiber Communication Conference*, pp. 1–4, 2011.
- [10] R. Soref and J. Lorenzo, "Single-crystal silicon: a new material for 1.3 and 1.6 μm integrated-optical components," *IET Electron. Lett.*, vol. 21, no. 21, pp. 953–954, 1985.
- [11] W. Bogaerts, R. Baets, P. Dumon, V. Wiaux, S. Beckx, D. Taillaert, B. Luyssaert, J. Van Campenhout, P. Bienstman, and D. Van Thourhout, "Nanophotonic waveguides in silicon-on-insulator fabricated with cmos technology," *IEEE J. of Lightw. Technol.*, vol. 23, no. 1, pp. 401–412, 2005.
- [12] U. Fischer, T. Zinke, J.-R. Kropp, F. Arndt, and K. Petermann, "0.1 db/cm waveguide losses in single-mode soi rib waveguides," *IEEE Photon. Technol. Lett.*, vol. 8, no. 5, pp. 647–648, 1996.

- [13] S. Assefa, S. Shank, W. Green, M. Khater, E. Kiewra, C. Reinholm, S. Kamalapurkar, A. Rylyakov, C. Schow, and F. Horst, "A 90nm cmos integrated nanophotonics technology for 25gbps wdm optical communications applications," in *IEEE International Electron Devices Meeting (IEDM)*, pp. 3–5, 2012.
- [14] H. Rong, A. Liu, R. Jones, O. Cohen, D. Hak, R. Nicolaescu, A. Fang, and M. Paniccia, "An all-silicon raman laser," *Nature*, vol. 433, no. 7023, pp. 292–294, 2005.
- [15] H. Rong, R. Jones, A. Liu, O. Cohen, D. Hak, A. Fang, and M. Paniccia, "A continuous-wave raman silicon laser," *Nature*, vol. 433, no. 7027, pp. 725–728, 2005.
- [16] T. Yin, R. Cohen, M. M. Morse, G. Sarid, Y. Chetrit, D. Rubin, and M. J. Paniccia, "31 ghz ge nip waveguide photodetectors on silicon-on-insulator substrate," *Opt. Expr.*, vol. 15, no. 21, pp. 13 965–13 971, 2007.
- [17] S. Assefa, F. Xia, S. W. Bedell, Y. Zhang, T. Topuria, P. M. Rice, and Y. A. Vlasov, "Cmos-integrated high-speed msm germanium waveguide photodetector," *Opt. Expr.*, vol. 18, no. 5, pp. 4986–4999, 2010.
- [18] A. Liu, R. Jones, L. Liao, D. Samara-Rubio, D. Rubin, O. Cohen, R. Nicolaescu, and M. Paniccia, "A high-speed silicon optical modulator based on a metal-oxide-semiconductor capacitor," *Nature*, vol. 427, no. 6975, pp. 615–618, 2004.
- [19] L. Liao, D. Samara-Rubio, M. Morse, A. Liu, D. Hodge, D. Rubin, U. D. Keil, T. Franck *et al.*, "High speed silicon mach-zehnder modulator," *Opt. Expr.*, vol. 13, no. 8, pp. 3129–3135, 2005.
- [20] Q. Xu, D. Fattal, and R. G. Beausoleil, "Silicon microring resonators with 1.5- μm radius," *Opt. Expr.*, vol. 16, no. 6, pp. 4309–4315, 2008.
- [21] T. Y. Ang, S. T. Lim, S.-Y. Lee, C. E. Png, and M.-K. Chin, "Polarization independent micro-ring resonators on submicron silicon-on-insulator (soi) rib waveguides," pp. 111–113, 2008.
- [22] G. Cao, L. Dai, Y. Wang, J. Jiang, H. Yang, and F. Zhang, "Compact integrated star coupler on silicon-on-insulator," *IEEE Photon. Technol. Lett.*, vol. 17, no. 12, pp. 2616–2618, 2005.
- [23] I. Solomon, R. Narendran, and B. K. Das, "Design and fabrication of integrated optical 1×8 power splitter in soi substrate using large cross-section single-mode waveguides," vol. 8173, 2010.
- [24] M. K. Smit and C. Van Dam, "Phasar-based wdm-devices: Principles, design and applications," *IEEE J. of Sel. Topics in Quant. Electron.*, vol. 2, no. 2, pp. 236–250, 1996.
- [25] B. G. Lee, A. Rylyakov, W. M. J. Green, S. Assefa, C. W. Baks, R. Rimolo-Donadio, D. Kuchta, M. Khater, T. Barwicz, C. Reinholm, E. Kiewra, S. Shank, C. Schow, and Y. A. Vlasov, "Four- and eight-port photonic switches monolithically integrated with digital cmos logic and driver circuits," in *Optical Fiber Communication Conference/National Fiber Optic Engineers Conference*, 2013.

- [26] P. Trinh, S. Yegnanarayanan, F. Coppinger, and B. Jalali, "Silicon-on-insulator (soi) phased-array wavelength multi/demultiplexer with extremely low-polarization sensitivity," *IEEE Photon. Technol. Lett.*, vol. 9, no. 7, pp. 940–942, 1997.
- [27] B. Jalali, S. Yegnanarayanan, T. Yoon, T. Yoshimoto, I. Rendina, and F. Coppinger, "Advances in silicon-on-insulator optoelectronics," *IEEE J. of Sel. Topics in Quant. Electron.*, vol. 4, no. 6, pp. 938–947, 1998.
- [28] R. Chuang, M.-T. Hsu, Y.-C. Chang, Y.-J. Lee, and S.-H. Chou, "Integrated multimode interference coupler-based mach-zehnder interferometric modulator fabricated on a silicon-on-insulator substrate," *IET Optoelectron.*, vol. 6, no. 3, pp. 147–152, 2012.
- [29] G. R. Bhatt, R. Sharma, U. Karthik, and B. K. Das, "Dispersion-free SOI interleaver for DWDM applications," *IEEE J. of Lightw. Technol.*, vol. 30, no. 1, pp. 140–147, Jan. 2012.
- [30] M. Asghari and A. V. Krishnamoorthy, "Silicon photonics: Energy-efficient communication," *Nat. Photon.*, vol. 5, no. 5, pp. 268–270, 2011.
- [31] S. P. Chan, C. E. Png, S. T. Lim, G. T. Reed, and V. Passaro, "Single-mode and polarization-independent silicon-on-insulator waveguides with small cross section," *IEEE J. of Lightw. Technol.*, vol. 23, no. 6, p. 2103, 2005.
- [32] W. R. Headley, G. T. Reed, F. Gardes, A. Liu, and M. Paniccia, "Enhanced polarization-independent optical ring resonators on silicon-on-insulator," in *Integrated Optoelectronic Devices*, pp. 195–202, 2005.
- [33] I. Kiyat, A. Aydinli, and N. Dagli, "A compact silicon-on-insulator polarization splitter," *IEEE Photon. Technol. Lett.*, vol. 17, no. 1, pp. 100–102, 2005.
- [34] K. Jinguji, "Synthesis of coherent two-port optical delay-line circuit with ring waveguides," *IEEE J. of Lightw. Technol.*, vol. 14, no. 8, pp. 1882–1898, Aug. 1996.
- [35] R. M. de Ridder and C. G. Roeloffzen, "Interleavers," in *Wavelength Filters in Fibre Optics*. Springer, pp. 381–432, 2006.
- [36] L. Vivien, S. Laval, B. Dumont, S. Lardenois, A. Koster, and E. Cassan, "Polarization-independent single-mode rib waveguides on silicon-on-insulator for telecommunication wavelengths," *Opt. Commun.*, vol. 210, no. 1-2, pp. 43 – 49, Sep. 2002.
- [37] R. K. Navalakhe, N. DasGupta, and B. K. Das, "Fabrication and characterization of straight and compact s-bend optical waveguides on a silicon-on-insulator platform," *Applied Optics*, vol. 48, no. 31, pp. 125–130, Nov. 2009.
- [38] H. Yamada, T. Chu, S. Ishida, and Y. Arakawa, "Si photonic wire waveguide devices," *IEEE J. of Sel. Topics in Quant. Electron.*, vol. 12, no. 6, pp. 1371 –1379, Dec. 2006.

- [39] R. A. Soref, J. Schmidtchen, and K. Petermann, "Large single-mode rib waveguides in GeSi-Si and Si-on-SiO₂," *IEEE J. Quant. Electron.*, vol. 27, no. 8, pp. 1971–1974, Aug. 1991.
- [40] Y. Quan, P. Han, Q. Ran, F. Zeng, L. Gao, and C. Zhao, "A photonic wire-based directional coupler based on soi," *Opt. Commun.*, vol. 281, no. 11, pp. 3105–3110, Jun. 2008.
- [41] S. T. Lim, C. E. Png, E. A. Ong, and Y. L. Ang, "Single mode, polarization-independent submicron silicon waveguides based on geometrical adjustments," *Optics Express*, vol. 15, no. 18, pp. 11 061–11 072, Sep. 2007.
- [42] K. Yamada, T. Tsuchizawa, T. Watanabe, H. Fukuda, H. Shinojima, and S. Itabashi, "Applications of low-loss silicon photonic wire waveguides with carrier injection structures," in *IEEE International Conference on Group IV Photonics*, pp. 1–3, 2007.
- [43] M. Bass, C. DeCusatis, G. Li, V. N. Mahajan, J. Enoch, and E. V. Stryland, *Handbook of Optics: Optical Properties of Materials, Non-linear Optics, Quantum Optics*, 1st ed. McGraw-Hill, 2009.
- [44] Rsoft BeamPROP, "www.rsoftdesign.com," 2008.
- [45] L. B. Soldano and E. C. Pennings, "Optical multi-mode interference devices based on self-imaging: principles and applications," *IEEE J. of Lightw. Technol.*, vol. 13, no. 4, pp. 615–627, 1995.
- [46] Lumerical MODE Solutions , "http://www.lumerical.com/mode.php." 2013.
- [47] R. K. Navalakhe, "Design, fabrication and characterization of straight and bend optical waveguides on silicon-on-insulator," Master's thesis, Dept. Electrical Engineering, IIT Madras, Jul. 2009.
- [48] A. Yariv and P. Yeh, *Photonics: Optical Electronics in Modern Communications (The Oxford Series in Electrical and Computer Engineering)*, 6th ed. Oxford University Press, USA, Jan. 2006.
- [49] G. T. Reed and A. P. Knights, *Silicon Photonics-An Introduction*. Wiley, 2004.
- [50] U. Karthik and B. K. Das, "Polarization-independent and dispersion-free integrated optical mzi in soi substrate for dwdm applications," *Proc. SPIE*, vol. 8629, 2013.
- [51] J. Song, Q. Fang, S. H. Tao, M. B. Yu, G. Q. Lo, and D. L. Kwong, "Proposed silicon wire interleaver structure," *Opt. Expr.*, vol. 16, no. 11, pp. 7849–7859, May 2008.

LIST OF PAPERS BASED ON THESIS

Journals/Proceedings

1. **U. Karthik**, and B.K. Das, "Polarization-independent and Dispersion-free integrated optical MZI in SOI Platform for DWDM applications", *Proc. SPIE*, 8629, 2013.
2. G.R. Bhatt, R. Sharma, **U. Karthik**, and B.K. Das, "Dispersion free SOI interleaver for DWDM applications", *J. Lightw. Technol.*, vol. 30, no. 1, pp. 140-147, Jan. 2012.

Conferences

1. **U. Karthik**, and B.K. Das, "Polarization-independent and Dispersion-free integrated optical MZI in SOI Platform for DWDM applications", *SPIE Photonics West*, San Francisco, USA, 2013.
2. B.K. Das, Sujith C., **U. Karthik**, "Silicon Photonics and Optical interconnect Technology", *ICOE - International Conference on Optical Engineering*, VTU, Belgaum, India, 2012.
3. B.K. Das, Sujith C., **U. Karthik**, "Research Advances in SOI Based Waveguide Sensors", *ICoNTOPTOP - Trends in Optics and Photonics II*, Kolkata, India, 2011.
4. B.K. Das, Sujith C., G.R. Bhatt, **U. Karthik** and R. Sharma, "Silicon Photonics in SOI platform: Problems with waveguide dispersion and birefringence effects", *Frontiers in Optics and Photonics*, New Delhi, India, 2011.

GENERAL TEST COMMITTEE

- CHAIR PERSON(s)** : **Prof. E. Bhattacharya**
The Head,
Dept. of Elec. Engg.
- Prof. Hari Shankar Ramachander**
Dept. of Elec. Engg.
- GUIDE** : **Dr. B.K. Das**
Dept. of Elec. Engg.
- GTC MEMBERS** : **Dr. Deepa Venkitesh**
Dept. of Elec. Engg.
- Prof. C. Vijayan**
Dept. of Physics

CURRICULUM VITAE

NAME : Uppu Karthik

DATE OF BIRTH : 19th Jan. 1989

EDUCATIONAL QUALIFICATIONS :

Master of Science (by Research), 2010-2013

Silicon Photonics

Dept. of Electrical Engineering, IIT-Madras

Chennai 600036, Tamil Nadu, India

Bachelor of Technology, 2006-2010

Electronics and Communications

St. Martin's Engineering College, JNT. University

Hyderabad, India